IGC Newsletter

INDIRA GANDHI CENTRE FOR ATOMIC RESEARCH

Technical Articles

- Synthesis of Novel Transition Metal Carbides at High Pressure and Temperature

- Online APAR Work Process Implementation with Digital Signature

Young Officer's Forum

- Radio-Frequency Alternating Magnetic Field Induced Heating of Magnetic Nanofluids: Magnetic Fluid Hyperthermia

Young Researcher's Forum

- CFD Investigations of Thermal Hydraulic Characteristics and Consequences of Flow Blockage in Fast Reactor Fuel Subassemblies
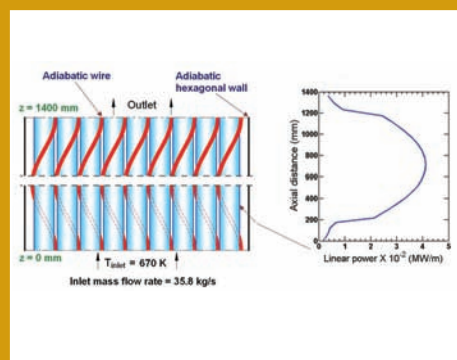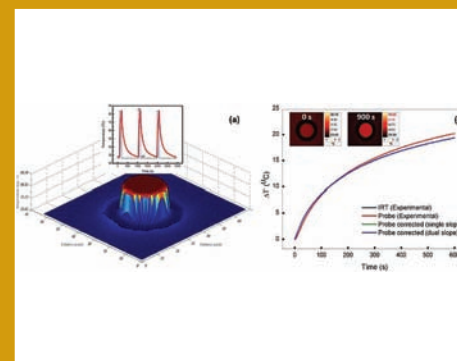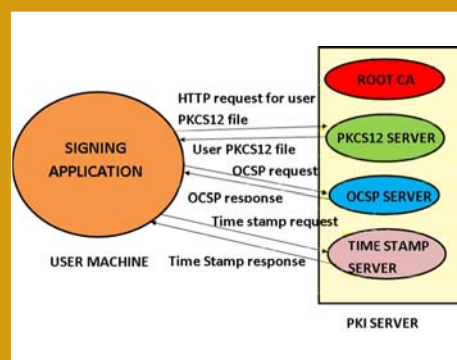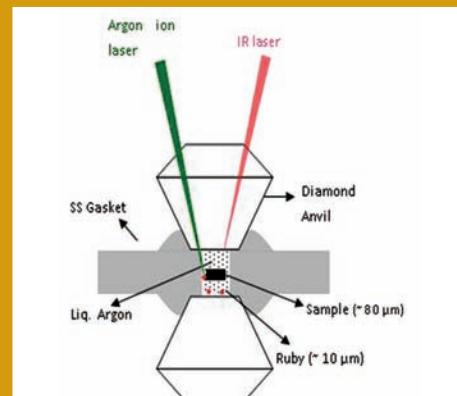
Conference and Meeting Highlights

- A brief report on one day Training Program on Quality Assurance Aspects for Engineers and Supervisors

- International Women's Day & The International Year of Periodic Table-2019

News and Events

HBNI-IGCAR Corner

Awards & Honours

From the Editorial Committee

Dear Reader

It is our pleasant privilege to forward a copy of the latest issue of IGC Newsletter (Volume 120, April 2019 issue).

In the first technical article Dr. N. R. Sanjay Kumar & colleagues, from Materials Science Group have described about the "Synthesis of Novel Transition Metal Carbides at High Pressure and Temperature".

In the second technical article Shri R. Jehadeesan & colleagues from Electronics and Instrumentation Group have described about the "Online APAR Work Process Implementation with Digital Signature".

This issue's Young Officer's Forum features an article by Dr. B. B. Lahiri from Metallurgy and Materials Group on the Radio-Frequency Alternating Magnetic Field Induced Heating of Magnetic Nanofluids: Magnetic Fluid Hyperthermia.

Shri M. Naveen Raj has discussed about the CFD Investigations of Thermal Hydraulic Characteristics and Consequences of Flow Blockage in Fast Reactor Fuel Subassemblies in the Young Researcher's Forum.

We are happy to share with you the awards, honours and distinctions earned by our colleagues.

We look forward to your comments, continued guidance and support.

With best wishes and personal regards

Editorial Committee, IGC Newsletter

Synthesis of Novel Transition Metal Carbides at High Pressure and Temperature

The driving force in the field of high pressure research has been the search for new super-hard materials with improved chemical and thermal stability comparable to or more than that of diamond. Super hard materials are those whose hardness is above 40 GPa. Hardness of diamond is about 90 GPa. There are three generic conditions that are to be met for a material to be hard namely, (a) it must have high bulk modulus i.e., it should resist volume deformation, (b) it should not deform in a direction different from the applied load i.e., it should have high shear modulus and (c) it should not undergo plastic deformation. Various approaches are adopted in the quest for superhard material and they can be broadly classified into three types, (i) Specific covalent substances, including various crystalline and disordered carbon modifications (ii) Covalent and ionic-covalent compounds and (iii) Partially covalent compounds of transition metals (TM) with light elements. The first two approaches have compounds made up of C or C with other low z elements like N, B and O and these are basically attempts at mimicking the sort of bonding that exists in diamond. The systems explored by these approaches are nano polycrystalline diamond, BN, CN etc.

Compounds formed between TM and light elements like B, C, N and O have immense industrial applications due to their high hardness, high melting point, excellent thermal conductivity, good wear and corrosion resistance properties. This approach is essentially to have maximum valence electron charge density, basically contributed by the TM, and forming p-d hybridized covalent bond between light elements C, B, N and TM respectively leading to enhancement in hardness (Ru has the largest valence charge density among 4d TM and Os among all the TM's). For example ReB_2 is reported to be super hard with hardness of 48 GPa. Manganese, ruthenium and osmium have the highest charge density among 3d, 4d & 5d TM's respectively. Also osmium is the least compressible metal with bulk modulus of 405 GPa. Hence C incorporation in these metal lattices is expected to be promising in obtaining candidate systems for super hard material.

However, the elements from the earlier TM series form carbides at ambient pressure conditions whereas latter TM elements do not form carbides. This is related to the filling of the d electrons along the group. The effect of filling of the d electrons along the group can be seen in the elemental systems wherein they exhibit a parabolic
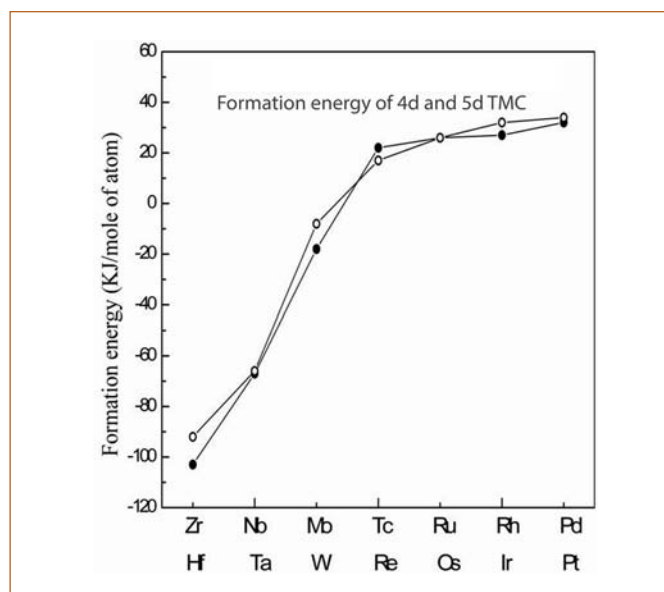

Figure 1: Formation energy of 4d and 5d transition metal carbides, filled circle and open circle symbol represent 4d and 5d TMC respectively

trend with respect to their atomic numbers in their physical properties like melting point, cohesive energy and bulk modulus. The formation energy predicted for 4d and 5d TM carbides by Miedema's semi-empirical method is plotted in Figure 1.

The formation energies for transition metal carbides become unfavorable in the latter part of the series. Under extreme conditions of high pressure and temperature, the nature of bonding in elements changes and the chemical reactivity increases such that direct elemental reaction even between the inert species is possible leading to the formation of novel and exotic phases. Also, high pressure synthesis in general leads to formation of dense phases. Thus it may be possible to synthesize these novel carbides under High Pressure High Temperature (HPHT) conditions, which otherwise are not possible by the conventional methods. Hence HPHT synthesis is attempted using Laser Heated Diamond Anvil Cell (LHDAC) technique.

Laser Heated Diamond Anvil Cell facility – HPHT synthesis

Laser Heated Diamond Anvil Cell (LHDAC) set-up is capable of subjecting samples simultaneously to HPHT conditions (P $\sim$ 100 GPa and T $\sim$ 5000 K) Principle of LHDAC is shown in Figure 2. The important components of the LHDAC set-up are 120 W continuous wave TEM_{00} mode CO_2
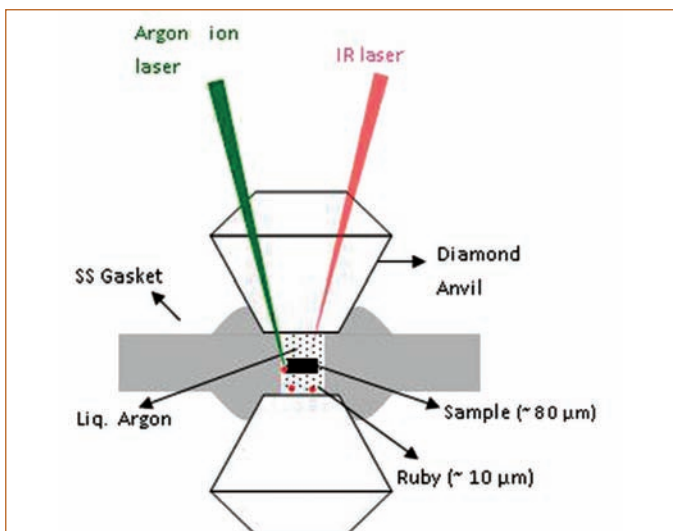
Figure 2: Diamond Anvils – Pressure generation, IR laser- heating, Ar ion laser – Ruby fluorescence, SS gasket – sample confinement, Ruby – pressure calibrant, Liq Argon – Pressure transmitting medium
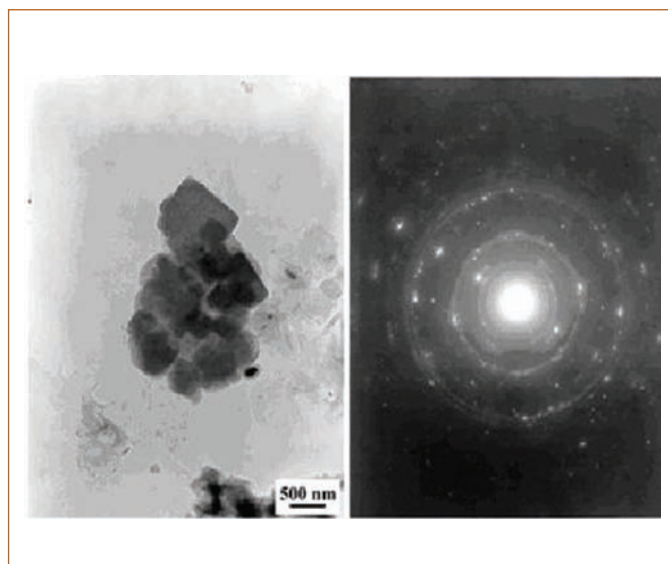

Figure 4: TEM bright field image and diffraction pattern from ruthenium carbide sample.

laser (λ = 10.6μm), He-Ne laser (λ = 632.8 nm), 5 W argon ion laser, optical components for IR beam steering and focusing, Mao-Bell type DAC, motorized XYZ translation stage, CCD based spectrometer and imaging system.

Sample assembly is crucial for successful HPHT synthesis experiments, in all the runs where we have used 1:4 ratio of TM:C. Finely powdered mixture of TM and C is pelletized and a small piece of this sample ~ 80 micron is placed in the sample chamber as

Figure 3: XRD patterns of laser heated samples, with both LN$_2$ and argon as PTM, * implies new reflections.

shown in Figure 2. Along with the sample, ruby (Al_2O_3:Cr^{3+}) specs are loaded which function as pressure calibrant, wherein the shift of the ruby fluorescence line with pressure is made use of. Finally the sample chamber is loaded with liquid Argon using an in-house developed cryogenic argon loading facility. Liquid Argon functions as Pressure Transmitting Medium PTM) and the choice of PTM is also dictated by the fact that it should not react with the sample at HPHT conditions. IR laser is focused on the pressurized sample contained in the DAC (spot size ~ 40 micron). The DAC stage mounted on XYZ stage is maneuvered so that uniform heating is carried out on the whole sample. Thermal spectra from the hot microscopic sample is collected through the optic fiber and fed into the spectrometer. The obtained spectra are then analyzed using either Planck's law or Wein's law to obtain temperature. Pressure measurement has been carried out by standard ruby fluorescence technique. The laser heated samples are characterized by High Pressure X Ray Diffraction (HPXRD), Transmission Electron Microscope (TEM) and Raman measurements.
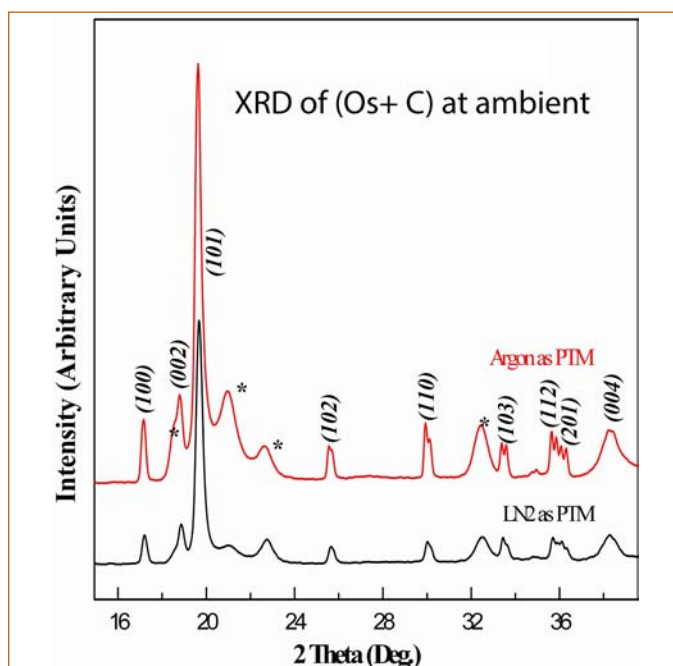
HPHT Synthesis of Novel Ruthenium and Osmium Carbide

Direct reaction between elements Ru:C and Os:C in the ratio 1:4 were carried out in the pressure range of 5 GPa to 8 GPa and temperature of ~ 2000 K. XRD before and after HPHT reveal reduction in intensity of the TM reflection and appearance of few new reflections. This indicates consumption of TM in the formation of Carbide. XRD pattern after HPHT for (Os + C) is shown in Figure 3 wherein appearance of four new reflections along with reflections of Os is seen. These reflections are seen in experiments carried
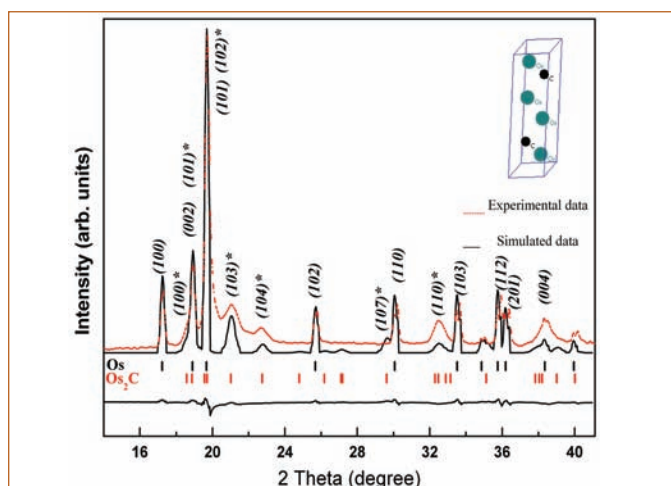
Figure 5: Experimental and simulated XRD plots for Os_2C. The inset shows the unit cell of Os_2C with space group $P6_3/mmc$.

out with liquid nitrogen and argon as PTM indicating that the synthesis is reproducible. Electron diffraction experiment on the retrieved HPHT treated sample were carried out and the Selected Area Diffraction (SAD) pattern of the (Ru+C) experiment is shown in Figure 4. In both these experiments, (Os + C) and (Ru + C), the reflections obtained from SAD correspond to those obtained from XRD.

From the new reflections obtained lattice parameter determination is carried out using indexing package POWD, hexagonal lattice parameter with a=2.534 Å, c=4.147 Å with V=23.05 Å^3 and $a =$ 2.536 Å, $c = 12.526$ Å with V = 69.8 Å^3 is obtained for ruthenium carbide and osmium carbides respectively.

Structure and stoichiometry determination of high pressure synthesized sample is difficult owing to the fact that synthesized sample has preferred orientation effects, micro-gram of synthesized sample along with presence of starting materials does not lend itself to density estimation and presence of starting materials rule out employing experimental techniques like Energy Dispersive Analysis by X-rays to estimate stoichiometry. In view of these facts, one looks for structures adopted by similar systems to be evaluated as candidate structure type. It is seen that mono-carbides of group IVA, VA and VIA adopts cubic lattice with the exception of MoC and WC, which are found in hexagonal lattice. First principle calculations predict NiAs and CoSn structure types for OsC. However, theoretical diffraction patterns were generated for the above probable structure types for hexagonal lattice for mono-carbide of Ru and Os, but they do not correspond to the experimental pattern. Hence RuC and OsC as possible compounds synthesized are ruled out. This can be understood from the fact

that enthalpy of formation is favorable for compositions which are metal rich rather than carbon rich. Recently high pressure synthesis of metal rich phases of nitrides and carbides of rhenium and iridium have been reported. In view of these facts, a closer look at the phase diagram of transition metal carbides of the type TM_2C reveals that these systems predominantly adopt the following space groups: $P3_121$ (152), $P\text{-}3m1$ (164), $P\text{-}6m2$ (187) and $P6_3/mmc$ (194). First principle electronic structure calculations have been carried out on Ru_2C and Os_2C for the above mentioned structure types to calculate the total energy and the electronic structure. Computation using density functional perturbation theory has also been carried out to calculate the phonon dispersions for all the candidate structures to determine the dynamic structural stability. Comparing the relaxed lattice parameter from the calculations with those obtained from the experiments and also examining the dynamic structural stability by phonon dispersions it can be concluded that the novel carbides synthesized, Ru_2C and Os_2C are in hexagonal structure with space group 164 and 194 respectively. The calculated and the experimental XRD patterns match well and simulated pattern for Os_2C in space group $P6_3/mmc$ (No.194) is shown in Figure 5. Calculations also indicate novel Ru_2C and Os_2C are metallic in nature.

Apart from synthesis of these novel TMC's it is interesting to know the mechanical properties, hardness, of these novel systems. As the sample quantity is only of few micro grams along with the presence of the starting elements it is not possible to measure hardness by standard nano indentation technique. Hence a semi empirical method wherein the crystal structure parameter is used to estimate hardness is employed. From this we estimate the hardness of Ru_2C and Os_2C to be ∼ 6 and 22 GPa respectively. Os_2C has higher hardness as compared to Ru_2C as in Os_2C, Os-C bond is shorter than that of C-C leading to higher degree of covalency.

HPHT Synthesis of Novel Manganese monocarbide (MnC) – potential super hard phase

Manganese (Mn) has the highest valence number among 3d transition metals. In the binary phase diagram of Mn and C, the phases reported are $Mn_{23}C_6$, Mn_5C_2, Mn_7C_3 and Mn_3C. The enthalpy of formation of MnC is positive. Hence we can expect the synthesis to be attainable by HPHT method. High pressure synthesis experiments with Mn:C in the ratio 1:5 were carried out in the pressure range of 5 to 10 GPa and temperature ∼ 2000 K. Several new reflections along with reduction in intensity of Mn
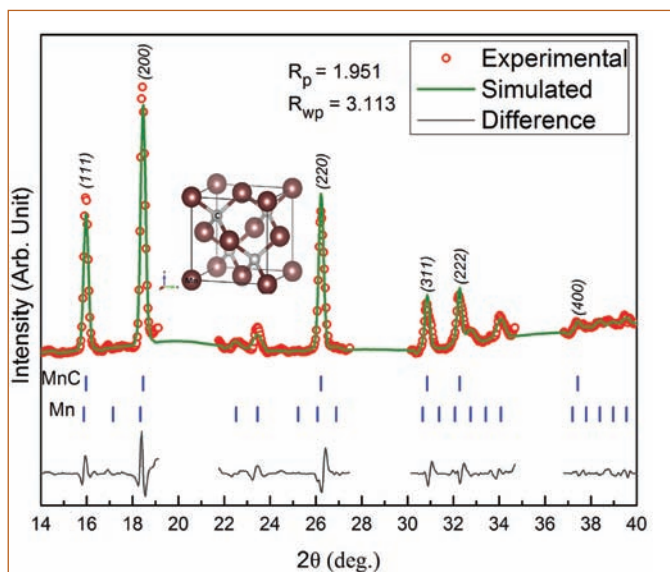
Figure 6: Le Bail fitting of the experimental MnC XRD pattern with ZnS structure type. The inset shows the unit cell of MnC (bigger sphere – Mn and smaller sphere – C). The blank regions of 2θ in the XRD plot are the regions which were excluded during Le Bail fitting due to presence of gasket peaks over there.

reflections are seen in the XRD and these results are corroborated by TEM measurements. Lattice determination is carried out using indexing package POWD, cubic lattice parameter with a = 4.42 Å is obtained with good figure of merit. The candidate structure types for cubic lattice of manganese carbide are Ag_2O, Nb_4C_3, ZnS and NaCl. Calculations as described earlier are carried out for these structures and the relaxed parameters obtained are 4.083 Å, 3.932 Å, 4.005 Å and 4.29 Å respectively. The experimental and computed lattice parameters are in reasonable agreement for cubic ZnS type structure (space group F-43m) as compared to other structure
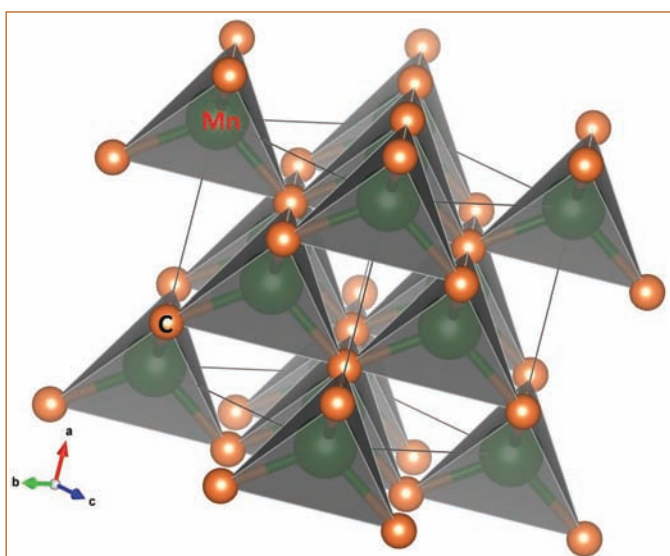

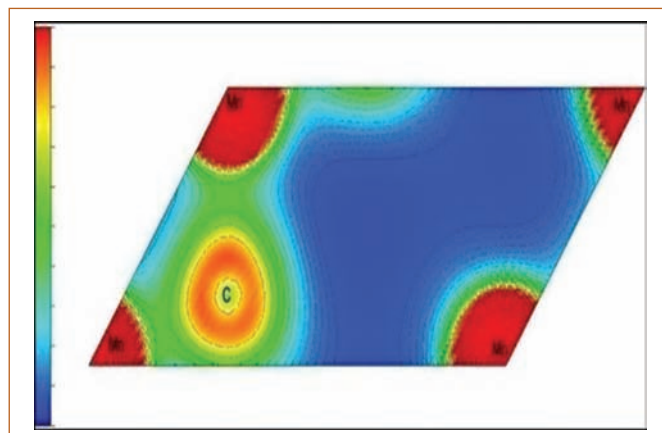Figure 7: Extended unit cell showing tetrahedral arrangement in MnC in ZnS structure.

Figure 8: Electronic charge density plot for the (1-10) plane of MnC, Mn atoms are in the corner

types and hence those are ruled out as probable structures for manganese carbide. Phonon dispersion calculation indicates existence of imaginary phonon modes for the calculated lattice parameter of ZnS structure of MnC. However phonon dispersion calculations indicate that at -20 GPa the structure is stable and also the corresponding lattice parameter at -20 GPa is in excellent agreement with that of experimentally obtained value. Le Bail fitting of the experimentally obtained pattern for ZnS type structure with the computed lattice parameters at -20 GPa is shown in Figure 6, thus leading to the conclusion that HPHT synthesized novel MnC is a high temperature phase adopting Cubic ZnS structure type.

From semi empirical methods, hardness of the novel MnC is estimated to be ~ 41 GPa making it a super hard material. To understand the high value estimated we compare it with the hardness of TiC and VC wherein both of them adopt NaCl structure. For TiC, the Ti-C bond length is 2.162 Å and the corresponding hardness is 16.4 GPa. Similarly for VC the bond length is 2.08 Å and the hardness is 25.4 GPa. From Figure 7 and 8 super hard property of MnC can be inferred to be arising due to high valence electron density of Mn, the short bond length (1.918 Å) and the tetrahedral arrangement in ZnS type MnC.

From the above results, it can be asserted that novel super hard material can be synthesized at a reasonably low pressure of 5 GPa. This paves way for bulk synthesis by multi-anvil apparatus which have huge industrial applications like cubic boron nitride, tungsten carbide and silicon carbide.

Reported by
N.R. Sanjay Kumar & colleagues,
Materials Science Group

Online APAR Work Process implementation with Digital Signature

A web portal has been developed to make online the work processes involved in submission, assessment, review & acceptance of Annual Performance Appraisal Report (APAR). The workflow is integrated with digital signature scheme to make the entire process (from initiation to completion) paperless and secure. The overall workflow of online APAR package is depicted in Figure1.

APAR Application Portal

The application portal has been developed in-house using the open source packages. The portal consists of following sub modules:

Self Appraisal Module

The module facilitates the employee to fill the self-appraisal part of the specified APAR form decided based on pay level and category. The employee personal information and leave details are automatically fetched from the personal database and displayed in the portal. The work tasks & accomplishments entered by the employee are validated against the predefined character limits and types mentioned in the APAR template. After successful validation the APAR contents are encrypted and saved in database and also embedded in APAR template PDF. The final self appraisal part of APAR in PDF format is signed digitally by the employee and securely forwarded to respective reporting officer for assessment.

Assessment Module

The module facilitates the reporting officer to evaluate the work tasks & accomplishments of the employee and award the numerical grading. The grading awarded are validated, encrypted and stored in database. The assessed APAR contents in PDF is signed digitally by the reporting officer and forwarded automatically to respective reviewing officer.

Reviewing Module

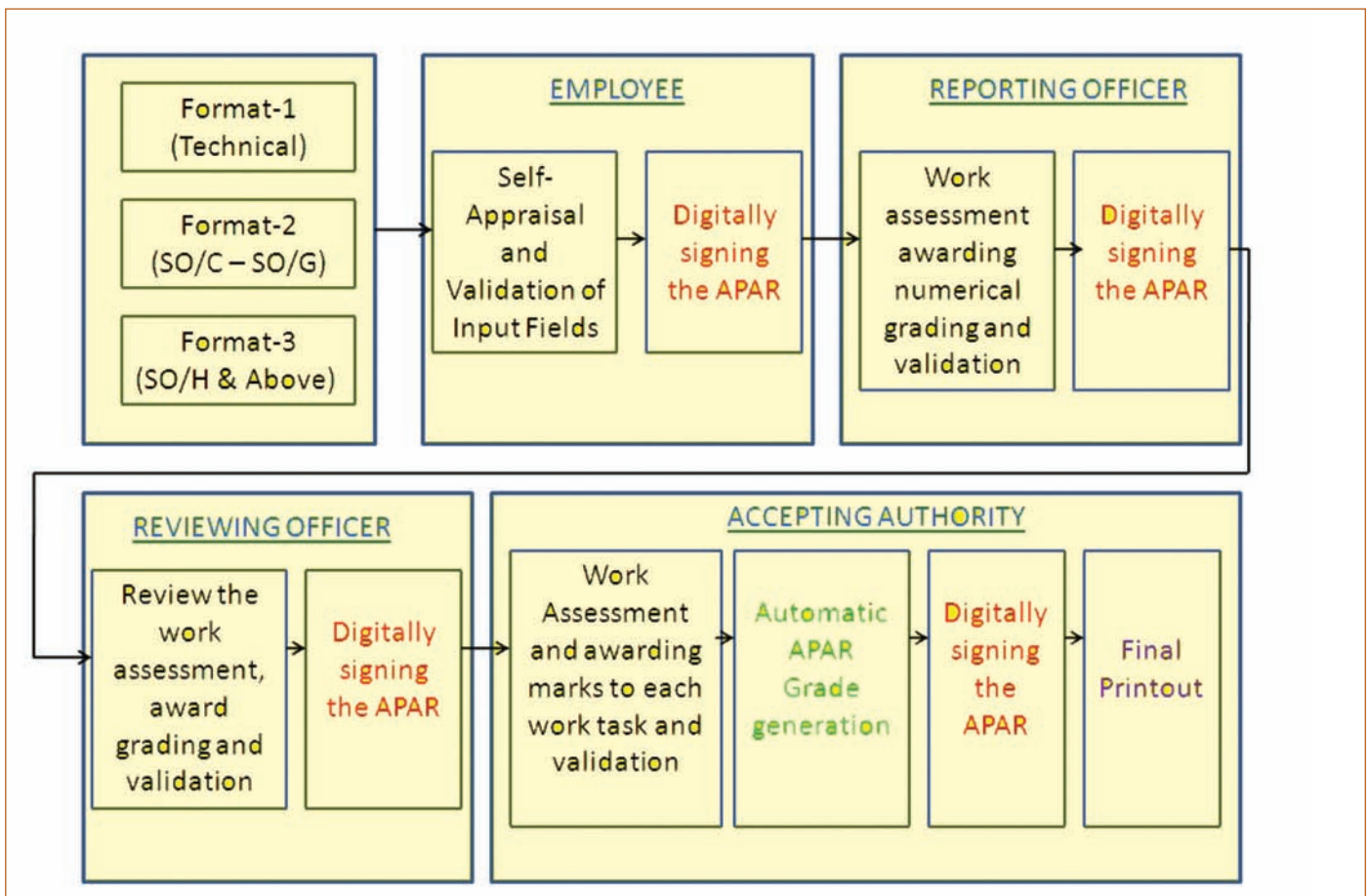The module facilitates the reviewing officer to review the assess-

Figure-1: Workflow of APAR Application Portal

ment of reporting officer and award the numerical grading on employee work accomplishments & personal attributes. The reviewed APAR in PDF is signed digitally and forwarded to respective accepting authority.

Accepting & Final Grading

The final acceptance module facilitates the accepting authority to view & award the final numerical grading. The numerical grading is automatically converted to actual APAR grading as per predefined conversion logic. The accepted APAR contents in PDF is signed digitally, encrypted and preserved in the database.

Analytics Module

A graphical drill-down analytics module has been developed for Head of Division/Associate director/Group director/Head of Unit to view the completion status, assessment & grading of the respective Division/Group/Unit in the capacity of accepting authority or higher. This helps in monitoring the submission, assessment and completion status of APAR and generate the statistics of grading in Section-wise, Division-wise or Group-wise manner.

All required security measures and access control restrictions are implemented to make sure that only authorized users with designated roles can access the relevant part of the APAR.

Management Module

The module facilitates the Group directors to add/update the reporting/reviewing/accepting authority details for each employee. If any of the employee records (like personal & leave details) have been updated in the centralized database server (ATOMS), it provides a facility to fetch the updates from the server on request to pre-fill the details in self appraisal form of the employee.

Digital Signature API module

An interface module has been developed to integrate with digital signature application to digitally fill and sign the APAR template in PDF format at each stage of APAR process (Self appraisal / Assessment/Reviewing / Accepting). It generates configuration files and interface data according to role of an employee (Self, Reporting/Reviewing/Accepting officer) and APAR format. The interface data will be communicated to the digital signature application running on user machine to embed the employee's digital signature in the PDF format of APAR.

Digital Signature Scheme

A digital signature is a mathematical technique used to validate the authenticity and integrity of a message, software or digital document. A valid digital signature gives a recipient reason to believe that the message was created by a known sender (authentication), that the sender cannot deny having sent the message (non-repudiation), and that the message was not altered in transit (integrity). For digital signature, user must have a private key and a public key. Private key is a binary code which is paired with another binary code called public key for setting off algorithms for message encryption and decryption. A digital signature is basically a fixed size unique binary representation of message, encrypted using user's private key which can be decrypted using user's public key to retrieve the original message. So, private key shall be retained by user alone for encryption whereas public key can be shared with other intended users for decryption. To implement this scheme in APAR workflow, a set-up technically termed as public key infrastructure (PKI) has been deployed in computer centre for creation, administration, distribution and revocation of digital certificates of all APAR users.

Public Key Infrastructure (PKI)

A public key infrastructure (PKI) is a set of roles, policies, and procedures needed to create, manage, distribute, use, store & revoke digital certificates and manage public-key encryption. PKI has been deployed on LINUX based server using OpenSSL components and in-house developed java applications and MySQL database.

Root Certifying Authority (Root CA)

The very first step to deploy PKI was to generate private-public keys of root certifying authority and generate root CA certificate. Subsequent to this the following procedures have been implemented on PKI server for generation of digital signature certificates (DSC) of users:

1. Key-pair generation - This component is responsible for creation of public-private key pair of the user using OpenSSL RSA algorithm with 2048 bits.

2. Certificate Signing request (CSR) generation –A CSR is generated using OpenSSL. CSR essentially contains user's public key and other information like user name, organization name, location etc. encrypted using user's private key.

3. User DSC certificate generation – This is performed by root CA. Root CA first verifies the CSR by decrypting user information using user's public key embedded in CSR. If verified correctly, CA signs the CSR information including user public key as well as additional CA related information. The CSR information along with CA signature is the user DSC which is encoded in standard X.509 format.

Public Key Cryptographic standards (PKCS) 12

The user DSC is combined with user private key into a PKCS12 format file and encrypted with a randomly generated default passphrase called PIN. A java application has been developed and implemented in the PKI server to automate the entire procedure for generation of digital signature certificates for users. This application facilitates generation of DSC of multiple users in one step by fetching relevant user information from MySQL database tables implemented in PKI server. The encrypted PKCS12 files of all users are stored in PKI server in a secured manner. A web service has been developed and deployed on PKI server for managing the transaction of these encrypted PKCS12 files between PKI server and user machine.

Revocation of Certificates and Online Certificate Status Protocol (OCSP)

There is a provision for revoking user certificate. This procedure has to be implemented when it is suspected that user passphrase has been compromised or when user forgets the passphrase. Once certificate is revoked it can no more be used for signing. For maintaining revocation status of certificates, OpenSSL Online Certificate Status Protocol (OCSP) component has been implemented. For this a private-public key pair of OCSP component is generated first, followed by its corresponding CSR generation. The CSR is then signed by root CA for generating DSC for OCSP. The OCSP component is then run as a service on a specific TCP/IP port in PKI server. The OCSP service waits for user OCSP request and sends the revocation status of user DSC to the client as soon as it receives any user request. The revocation status is encrypted with the private key of OCSP and sent to client along with OCSP public key. The entire OCSP unique resource locator (URL) is embedded in user certificates.

Secure Time Stamping Authority (TSA)

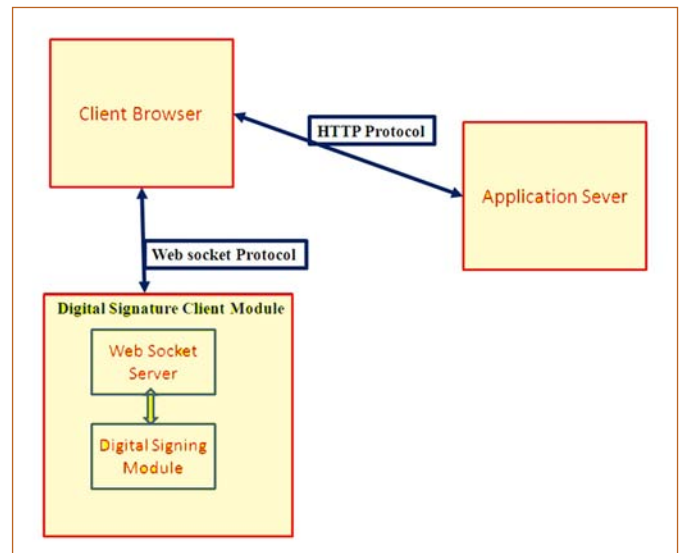Another important feature of digital signature is embedded secured

Figure 2: DSC Client Application interface scheme

timestamp. Secured timestamp when embedded into digital signature serves as secured proof of the time at which signing happened. This functionality is implemented by deploying OpenSSL time stamping component as a web service in PKI server. For implementing this service private-public key pair and DSC for TSA were generated. The service sends PKI server time encrypted with private key of timestamp server and TSA public key to the client.

Digital Signature Client Application (DSCA)

As per Controller of Certifying Authorities (CCA) the PIN used to encrypt the user digital certificate should not be communicated over the network. So a JAVA based Digital Signature Client Application (DSCA) has been developed in house to digitally sign PDF document on user machine itself. DSCA has to be installed on user computer for digitally signing APAR. The application runs as a service on user computer and enables the user to digitally sign APAR through browser. The java based service communicates with APAR portal in browser through "websocket" protocol.

WebSocket module

Websocket is a HTTP based protocol enabling browser based applications to communicate with other external applications in a client-server paradigm. The protocol is defined in a standard named RFC 6455. A java based websocket server library has been developed for enabling the digital signature client application to communicate with APAR portal running in browser. Similarly a javascript based websocket client library is implemented in APAR application to communicate with the signing application. The interfaces
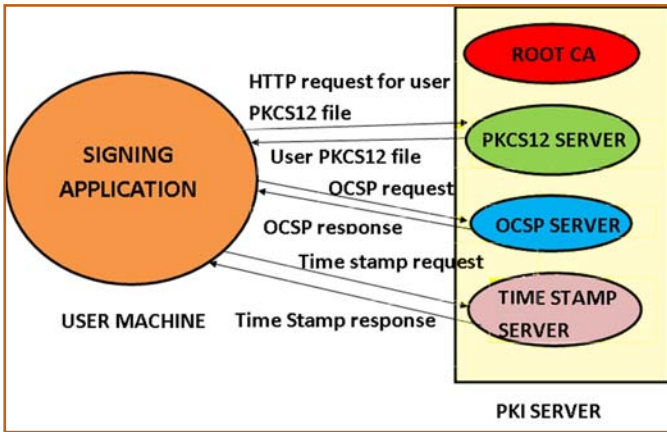
Figure 3: Signing application interface with PKI server

Figure 5: Digital Signature Certificate (DSC) PIN change portal

of APAR portal with its application server and DSCA is shown in Figure 2. The APAR portal fetches configuration files from the application server and sends to DSCA to initiate the process of digital signature.

Digital Signature Module

The digital signature module of DSCA gets the APAR PDF file from the application server and user PKCS12 file from PKI server as per the configuration data received from portal. It calculates the hash of the PDF content and prepares the message digest for signing. DSCA enables browser to prompt the user to enter the certificate PIN. The message digest is then encrypted with the user's private key decrypted from the PKCS12 file. It is then embedded in the specified portion of PDF. Along with the signed message digest, OCSP and TSA responses obtained from PKI server are also embedded into the signed document as part of signature.

Interfacing of DSCA with PKI server is shown in Figure 3. The signature also contains the entire certificate chain which is used by PDF readers for signature verification. The PKCS12 file of user is discarded from local memory after signature process is over. This module facilitates embedding of multiple signatures in a document. PDF reader verifies the signature based on certificate chain, em-

bedded revocation status and OCSP public key, embedded timestamp and TSA public key. If signature is verified successfully and certificate chain is trusted, signature on document appears with green tick mark as shown in Figure 4. The APAR application portal integrated with digital signature at each stage has been successfully developed and deployed for approximately 1800 users in IGCAR and GSO.

PIN change module

This module enables users to replace the default passphrase (PIN) of DSC files with PIN provided by user (Figure 5). This ensures the confidentiality of encrypted DSC file. The DSC file encrypted with default PIN is downloaded to the client computer by the client digital signature application. The file is decrypted and then re-encrypted with user specified PIN on the client machine. This file is then uploaded back to PKI server by the client application and discarded from local memory.

To summarize, an online APAR portal with digital signature scheme has been successfully designed, developed and deployed for IGCAR and GSO users. A PKI set-up comprising of in-house developed software and open source components have been established for facilitating digital signing of documents. Currently work is underway for integrating various other in-house portals with PKI. Also methodologies to implement PKI on Hardware Security Module (HSM) and storing DSC on hardware tokens are being explored for enhanced security of digital signature scheme.
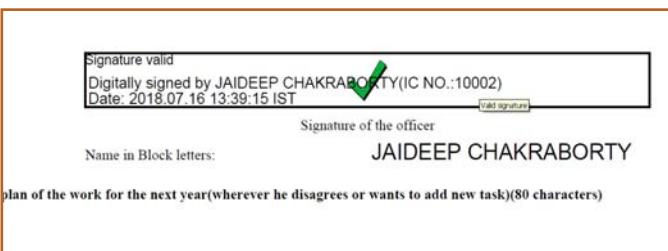

Figure 4: Digitally Signed APAR

Reported by
R.Jehadeesan & colleagues,
Computer Division/EIG

Young Officer's FORUM

Radio-Frequency Alternating Magnetic Field Induced Heating of Magnetic Nanofluids: Magnetic Fluid Hyperthermia

Dr. B. B. Lahiri is working in Smart Materials Section, CSTD, MMG, IGCAR. He is from the 53rd batch of BARC Training school, Mumbai. He acquired his M.Sc. in Physics from Jadavpur University, Kolkata and obtained his PhD from HBNI in 2018, under the guidance of Dr. John Philip. Dr. Lahiri's research interest include probing of magnetization dynamics at nanoscale, microscopic heat transfer mechanisms and developing infrared thermography based novel characterization techniques. He has 27 journal publications to his credit and is the recipient of DAE Young Applied Scientist/Technologist Award-2014.

Magnetic nanoparticles have found widespread applications in bio-medical fields. Magnetic fluid hyperthermia (MFH) is one such application, where a fluid containing magnetic nanoparticles (MNP) is injected into cancerous tissues and thereafter exposed to a radiofrequency alternating magnetic field (RFAMF), which causes a rise in the fluid or tissue temperature, due to the inherent Neel-Brown relaxation of the dispersed superparamagnetic MNP, leading to cellular degradation. The high surface to volume ratio of the surface modified MNP is found to be beneficial for preferential conjugation with tumor cells and external magnetic field guided drug delivery. Several in *vivo* and in *vitro* studies show good efficacy of MFH assisted cancer treatment. Owing to its immense clinical benefits, MFH is being considered as an alternate cancer treatment modality. Recently, multimodal hyperthermia therapy,

using larger sized magnetic nano-carriers, is demonstrated, where MFH is synergistically coupled with drug delivery or photodynamic therapy. Though RFAMF induced heating of MNP is well studied, several challenges still remain, like the effects of MNP concentration, dipolar interactions, size polydispersity, medium viscosity and external DC magnetic field induced texturing on heating efficiency are poorly understood. Figure 1 schematically shows the various influencing parameters for RFAMF induced heating of magnetic fluids and two major applications, viz. MFH and magneto-thermally
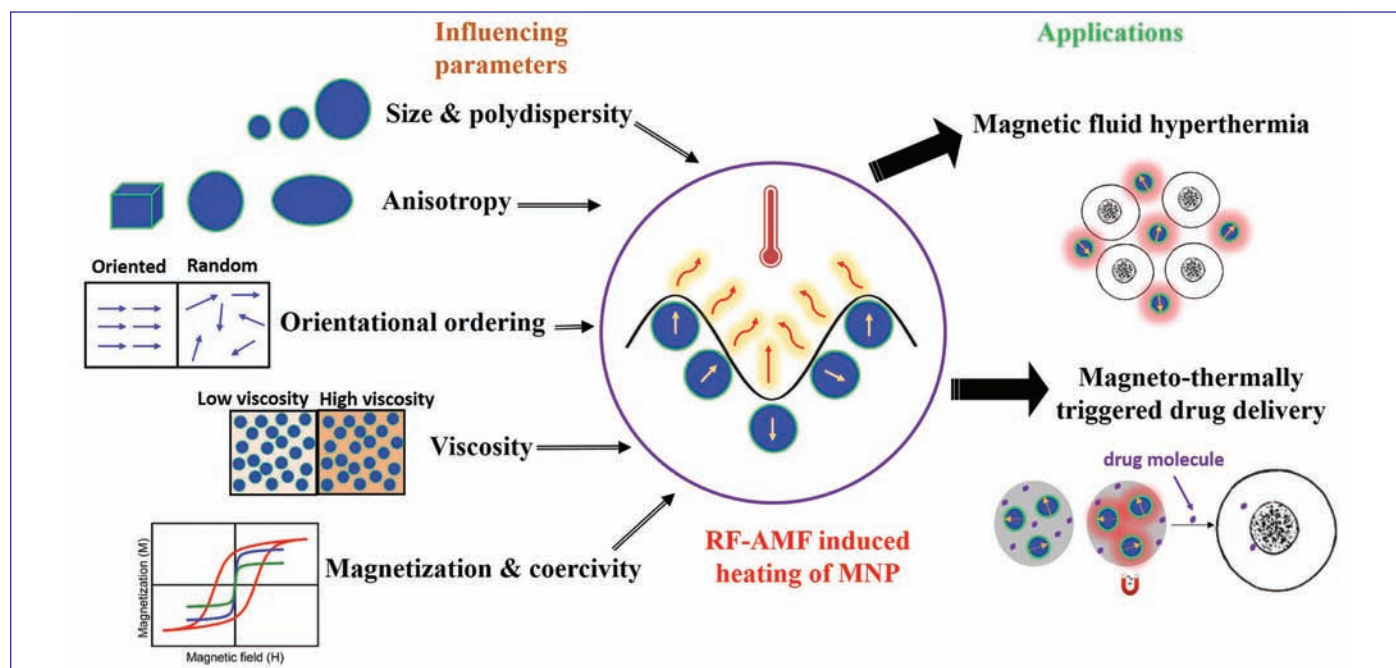
Figure 1: During RF-AMF induced heating, MNP act as efficient converters of magnetic energy to heat energy. Various factors (like size & polydispersity, anisotropy, orientational ordering, medium viscosity, saturation magnetization and coercivity) influencing RF-AMF induced heating efficiency in magnetic nanoparticles are schematically shown. Two major applications of RF-AMF induced heating of MNP, viz., magnetic fluid hyperthermia and magneto-thermally triggered drug delivery are also illustrated.

Figure 2: Photograph of the RF induction heating system used for magnetic fluid hyperthermia experiments. (a) Infrared camera, (b) fiber optic temperature sensor, (c) o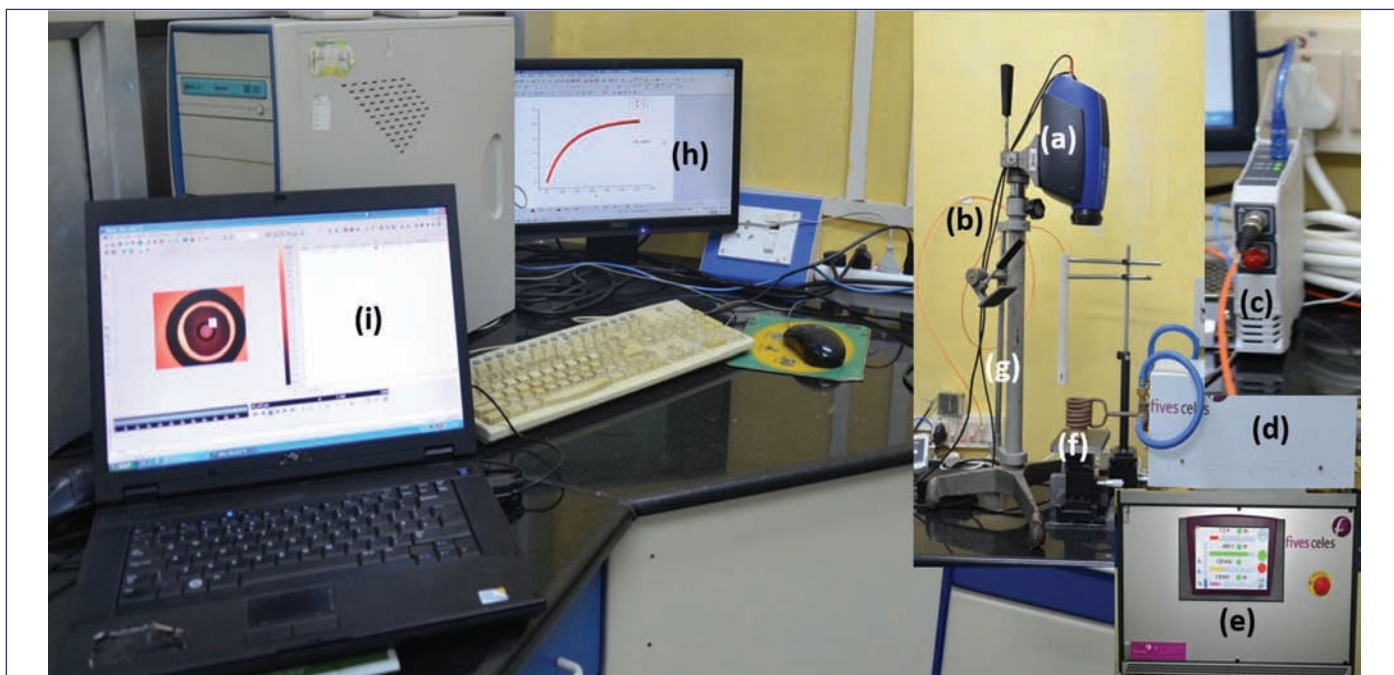ptical to electrical signal converter, (d) resonator tank, (e) high frequency generator, (f) heating coil, (g) tripod stand for infrared camera, (h-i) data acquisition systems. The sample is placed at the centre of the heating coil.

triggered drug delivery. In MFH, the heating efficiency is quantified in terms of a dosimetric quantity SAR (specific absorption rate), which is defined as the heating power per unit mass. Due to non-adiabatic experimental protocols, there are several uncertainties involved in SAR quantification, which have been rarely addressed. For real time *in vivo* applications of MFH in human, effective monitoring of temperature, preferably mapping, of the entire tumor region is required which warrants the need for developing a non-contact and wide area temperature mapping protocol. This calls for further investigations on the RFAMF induced heating of magnetic nanofluids and a detailed experimental study is undertaken, where the primary objectives are : i) to probe the role of MNP concentration, medium viscosity and size polydispersity on RFAMF induced heating efficiency; ii) to assess thermal losses associated with non-adiabatic experimental protocols and to develop a adiabatic reconstruction based data analyses method for accurate quantification of SAR; iii) to develop a non-contact temperature mapping protocol during RFAMF induced heating of magnetic fluid using infrared thermography (IRT) and convection correction data analyses method; (iv) to probe RFAMF induced heating in larger sized magnetic nanoemulsions from the perspective of multimodal therapy and (v) to study the effect of external DC magnetic field induced texturing on MFH efficiency of magnetic nanoemulsions.

Towards this goal, an infrared thermography (IRT) coupled RFAMF system, along with conventional temperature probe is established. A high frequency induction heating system that operates at a fixed frequency of 126 kHz and under varying field amplitudes (63.0-26.0 kA/m) is used as the RF source. This system facilitated simultaneous temperature measurement in contact (RF immune fiber optic temperature sensor) and non-contact modes, which made it a versatile and unique experimental facility for calorimetric as well as biological experiments. The induction heating system was equipped with a parallel resonance tank circuit and a water cooled electrolytic copper coil with 6 number of turns. Figure 2 shows a typical photograph of the experimental set-up. SAR was estimated from the initial rate of temperature rise under non-adiabatic limit, which was quantified by linear regression analysis of the initial data and also by using Box-Lucas method. For a non-adiabatic experimental set-up, a large amount of heat is lost to the surrounding and hence, only a part of the generated heat is actually responsible for increasing the sample temperature. Various thermodynamic uncertainties associated with peripheral heating, delayed heating, heat loss from sample and spatial variation in temperature profile within the sample were analyzed experimentally. An adiabatic reconstruction based data analysis protocol was developed for the accurate estimation of SAR, which was found to decrease the uncertainties by threefold. The
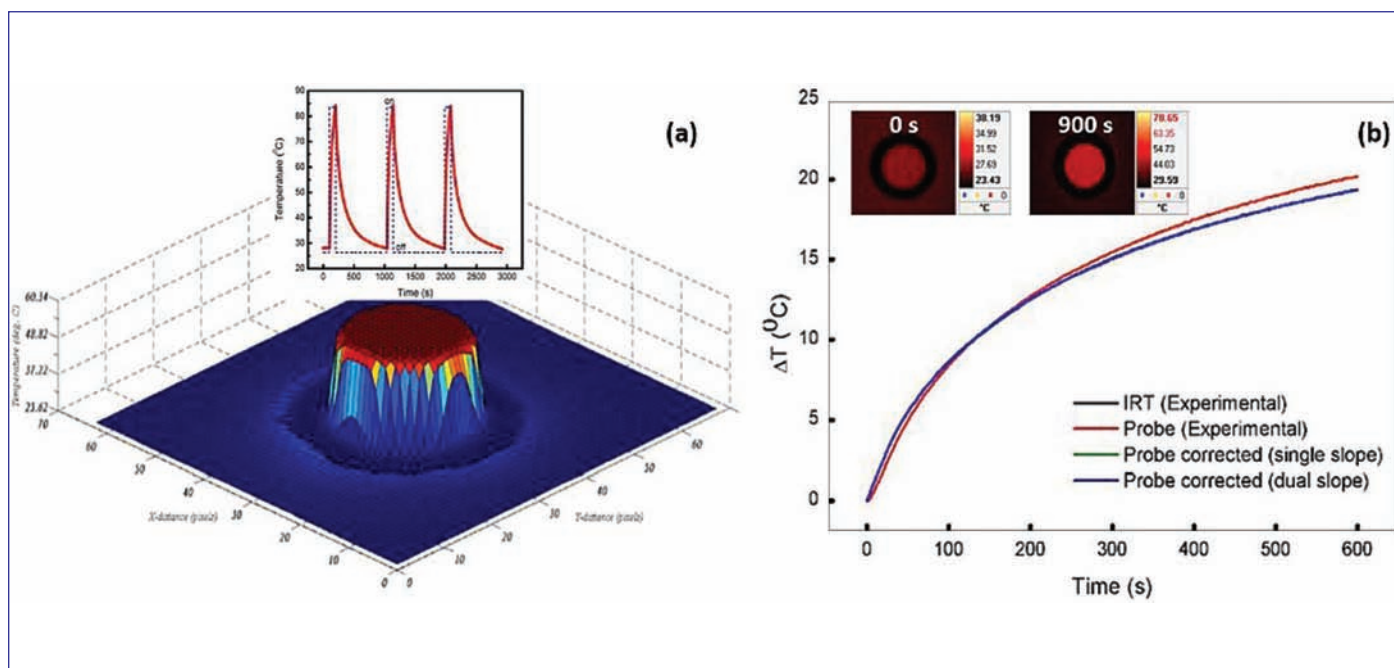
Figure 3: (a) 3-D surface plot for the oil based sample during RFAMF induced heating. (Inset) Thermal cycling showing repeatable thermal response of the magnetic nanofluid. (b) Convection correction data analysis protocol for the water based magnetic fluid. (Inset) Typical infrared images of the water based magnetic fluid during RFAMF (63.0 kAm[-1]) induced heating at time t = 0 and 900 s.

experiments were performed on in-house synthesized water and oil based magnetic fluids. The water based magnetic nanofluids contained tetramethyl ammonium hydroxide (TMAOH) coated Fe_3O_4 and phosphate capped Fe_3O_4 MNP. On the other hand, the oil based magnetic nanofluids contained oleic acid coated Fe_3O_4 dispersed in kerosene. The MNP were synthesized using standard chemical co-precipitation methods. The thin layers of phosphate, TMAOH or oleic acid coating provided electrostatic or steric stability in the water and oil media, respectively. Oil-in-water magnetic nanoemulsions were prepared using standard phase inversion, followed by fractionation method. The hexane oil droplets contained oleic acid capped Fe_3O_4 MNP, which were electrostatically stabilized in aqueous medium using sodium dodecyl sulphate. To study the effect of medium viscosity, the water based magnetic fluids were immobilized in an agar medium to experimentally simulate tissue like viscous environment. Immobilization in agar medium resulted in abrogation of Brownian relaxation, which drastically reduced the RFAMF induced heating efficiency. External DC magnetic field (H_{DC}) induced orientational ordering was achieved using two permanent magnet pole pieces and samples with three different orientations were prepared, viz. random orientation (H_{DC} = 0), parallel and perpendicular orientations with respect to the direction of RFAMF. The prepared samples were characterized using various in-house hosted experimental techniques, such as powder X-ray diffraction (XRD), small angle X-ray scattering (SAXS), dynamic

light scattering (DLS), thermogravimetric analysis (TGA), Fourier transform infrared spectroscopy (FTIR), vibrating sample magnetometer (VSM), atomic force microscopy (AFM) and magnetic force microscopy (MFM).

RFAMF induced heating in water and kerosene based magnetic nanofluids, containing TMAOH and oleic acid coated Fe_3O_4 MNP, respectively, was studied using infrared thermography (IRT). IRT based experiments enabled surface temperature mapping, which showed a uniform and homogenous temperature rise in the magnetic fluids during RFAMF induced heating. Figure 3a shows a typical 3D surface plot during RFAMF induced heating of the oil based sample. It was observed that the RFAMF induced temperature rise curves measured using fiber optic temperature sensor and IRT were remarkably similar. Nevertheless, IRT data indicated a higher initial rate of temperature rise and a lower maximum temperature at the end of the heating period, which were attributed to the internal and external convection phenomena, respectively. The temperature measurement performed using fiber optic temperature sensor reflected the internal fluid temperature, whereas IRT measured temperature over the entire area of the top surface of the fluid sample. During RFAMF induced heating, the heat generated by the MNP is dissipated into the base fluid, which resulted in rarefication of the base fluid that subsequently moved upwards due to buoyancy forces. On the other hand, due to incompressibility of the
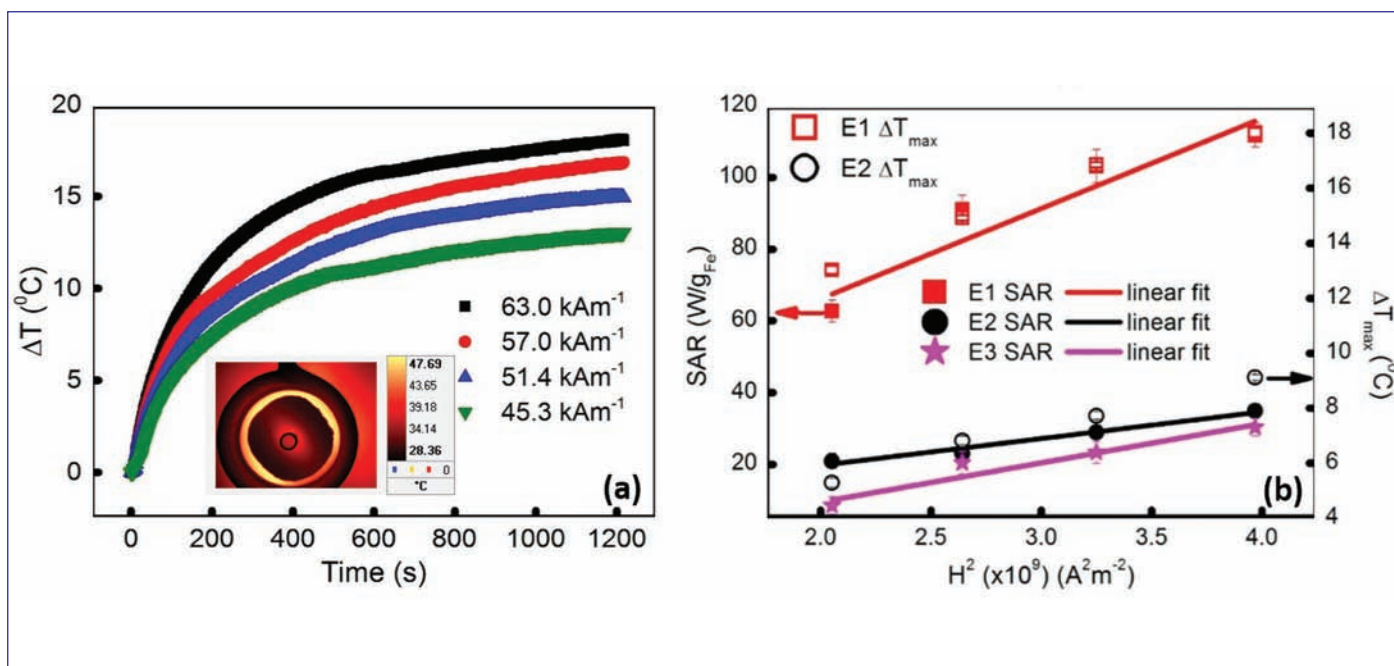
Figure 4: (a) Temperature rise, as a function of time for a typical emulsion sample during RFAMF induced heating under different external field amplitudes. (Inset) Typical infrared image of the emulsion sample during RFAMF induced heating. (b) Variation of SAR and ΔT_{max} as a function of H^2 for the magnetic nanoemulsions.

fluid, comparatively cooler fluid, being heavier, travelled downward due to gravity leading to a lower internal fluid temperature, as compared to the surface temperature (measured using IRT). Beyond certain time, as the temperature difference between the fluid and surrounding increased, external convection loss started primarily from the top surface of the fluid, which was exposed to the air. This caused the rate of temperature rise, measured using IRT, to decrease beyond certain time which resulted in a crossover of the IRT and fiber optic temperature sensor based curves. Beyond these crossover points the surface temperature rise measured using IRT was found to be lower compared to the rise in internal fluid temperature, where the convection losses were insignificant during the measurement time. The increasing and decreasing sections of the temperature difference (between IRT and fiber optic temperature sensor) curves were fitted with Box-Lucas and linear equations, respectively, and based on these calibration curves, an empirical data analysis procedure was developed for incorporating the convection phenomena. The convection corrected SAR values obtained from IRT were found to be in good agreement (maximum errors were limited within $\pm$ 5 %) with those obtained from fiber optic temperature sensor. Figure 3b shows the convection corrected data analysis protocol during RFAMF induced heating of the water based sample. In the case of water based magnetic fluids, the highest SAR was obtained as $\sim$ 135.9 ($\pm$ 4.6) W/

g_{Fe} for a sample concentration of 3 wt. %, under an external field amplitude of 63.0 KAm^{-1} and SAR was found to decrease with increasing sample concentration due to an enhancement in dipolar interaction, possibly due to slight aggregation. On the other hand, for oil based magnetic fluids, in the absence of agglomeration, enhancement of dipolar interaction was insignificant and SAR was found to increase with sample concentration due to an increase in the effective number of heat sources per unit volume. The highest SAR obtained in the case of oil based sample was $\sim$ 75.2 ($\pm$ 3.4) W/g_{Fe} for 23 wt. % concentration, under an external field amplitude of 57.3 kAm^{-1}. IRT based temperature measurement offers several advantages over conventional fiber optic temperature sensor based point measurements, viz., non-contact and real time temperature measurement, contamination free measurement and visualization of the entire surface temperature distribution. The developed convection correction protocol was successfully applied for water and oil based magnetic fluids, with significantly varying thermal diffusivity and Prandtl number, indicating the universal adaptability of IRT as an alternate temperature measurement methodology during MFH.

RFAMF induced heating in water based magnetic nanofluids containing phosphate coated superparamagnetic Fe_3O_4 MNP was studied experimentally. Phosphate coating makes the MNP

biocompatible and improves the stability of the MNP in aqueous medium at biologically relevant pH, which are beneficial for practical applications. The SAR values were determined from the initial rates of temperature rise and it was observed that SAR varied linearly with square of the external field amplitudes, in accordance with the Rosensweig's linear response model [$P=0.5\omega\mu_0\chi H^2\omega\tau(1+\omega^2\tau^2)^{-1}$] where P, χ, ω and τ indicate heating power, ensemble averaged equilibrium susceptibility, angular frequency and effective relaxation time, respectively]. It was further observed that, for the phosphate coated Fe_3O_4 MNP, SAR increased initially with sample concentration, attained a maximum at an optimum concentration and decreased thereafter with increasing sample concentration. The decrease in SAR beyond the optimum sample concentration was attributed to the enhancement of dipolar interaction and particle agglomeration. With increasing sample concentration, interparticle distance decreased resulting in an enhancement of dipolar interaction, which caused the anisotropy energy barrier to decrease. For a lower anisotropy barrier height, number of spin flips increased, albeit with a lower energy release per flip and SAR was optimum for the condition when the product of number of flips per unit time and energy release per flip was maximum. For higher sample concentration, enhancement of dipolar interaction resulted in reduced Neel relaxation time [$\tau_N = \tau_0\exp(KV_p/k_BT)$, where τ_0, K, V_p, k_B and T indicate attempt time, anisotropy energy density, volume of the MNP, Boltzmann's constant and sample temperature, respectively] and ensemble averaged equilibrium susceptibility, both of which contributed to the lowering of SAR.

In the case of MNP based nanofluids, the field induced heating is attributed to the Neel-Brown relaxation of the MNP under the influence of RFAMF. On the other hand, in oil-in-water magnetic nanoemulsions with MNP loaded in the oil phase, the RFAMF induced heating is due to Neel-Brownian relaxation of the MNP (length scale $\sim$ 10 nm) and whole scale Brownian relaxation of the emulsion droplets at 20 times larger length scale ($\sim$ 200 nm). Figure 4a shows the typical temperature rise curves during RFAMF induced heating of a magnetic nanoemulsion. The observed SAR of the magnetic nanoemulsion with similar size and MNP concentration but with different polydispersity showed that the sample with lower polydispersity ($\sigma = 0.2$) exhibited a significantly higher SAR, as compared to the sample with larger polydispersity ($\sigma = 0.4$), under identical experimental conditions. Here, σ indicates the standard deviation in the natural logarithm of the most probable size. Figure 4b shows the variation of SAR and ΔT_{max} as a function of the

square of the RFAMF amplitudes (H^2) for three different magnetic nanoemulsions. The SAR obtained for a sample with 4.6 wt. % MNP loading (with $\sigma = 0.4$) and 1.7 wt. % MNP loading (with $\sigma = 0.3$) were comparable, indicating that higher MNP loading does not necessarily result in a higher SAR in polydisperse system. The contributions from the whole-scale Brownian relaxation of the emulsion droplets was eliminated by immobilizing the droplets in an agar matrix (4 wt. % agar concentration). The maximum SAR for the immobilized sample was 41.7 $\pm$ 2.4 W/g_{Fe}, as compared to the significantly higher value of 111.8 $\pm$ 3.4 W/g_{Fe}, observed for the emulsion droplets dispersed in water. The observed reduction in SAR by $\sim$ 40-50 % in agar immobilized emulsion sample was attributed to the abrogation of Brownian relaxation.

Studies on the effect of external DC magnetic field induced orientational ordering on MFH efficiency of the agar immobilized emulsion droplets showed that the formation of linear chain-like structures due to head-on aggregation of the emulsion droplets along the direction of the external DC magnetic field, which were confirmed using AFM, led to an increase in heating efficiency. Figures 5a-b show the AFM topography images of the oriented magnetic nanoemulsion droplets. Magnetic force microscopy (MFM) studies showed the presence of emulsion droplets from the MFM phase contrast image (Figure 5c). Using classical point dipole approximation, the residual volume magnetization of the emulsion droplets was found to be $\sim$ 1.1 $\times$ 10^{-6} emu/cc, indicating the superparamagnetic nature of the emulsion droplets even after disorder-order transition. For a fixed amplitude of RFAMF, SAR was found to be higher for the sample oriented parallel to the direction of RFAMF due to an increase in the effective uniaxial anisotropy energy density along the chain direction, resulting in a higher effective relaxation time. Theoretical calculations of the total energy (consisting of the Zeeman and anisotropy energy terms) indicated an increase of effective uniaxial anisotropy energy density for the parallel orientation ($\sim$ 3 times higher than the perpendicular orientation) leading to an increase in effective relaxation time (Neel dominated) and a higher SAR for the sample with parallel orientation. Figure 5d shows a bar chart comparing the SAR values of the magnetic nanoemulsion under three different orientation, viz. parallel, perpendicular and random.

The key findings of the study are summarized below:

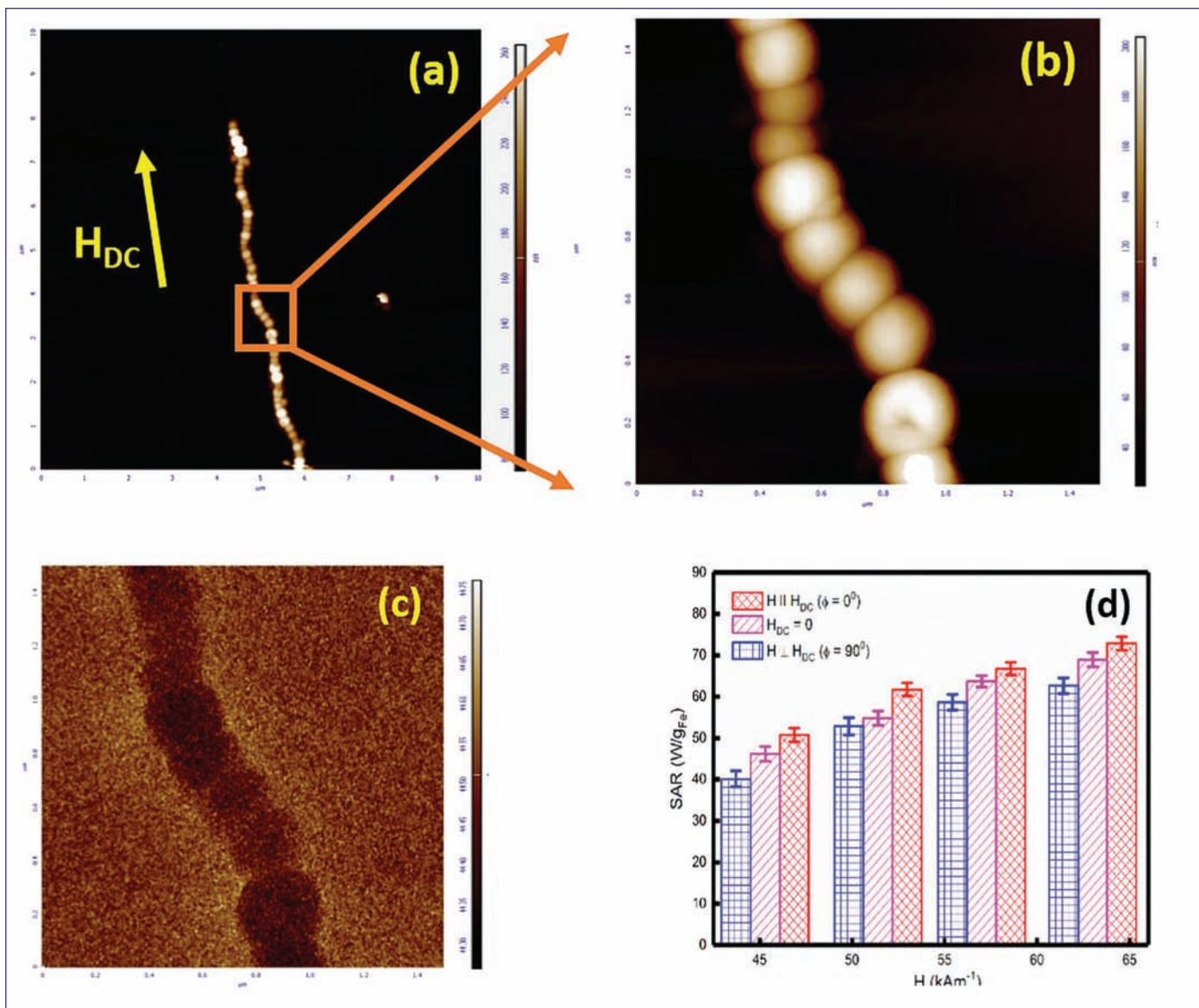Magnetic fluid hyperthermia set-up coupled with IRT based non-

Figure 5: (a) AFM topography image showing orientational ordering under the influence of an external DC magnetic field (shown by the arrow). (b) Magnified view of a section of figure (a). (c) MFM phase contrast image of figure (b). (d) A bar chart showing the SAR values of the emulsion samples for parallel, perpendicular and random orientations.

contact temperature mapping and convection correction data analysis protocol was developed, which established the efficacy of IRT for the accurate estimation of heating efficiency. This is an important step towards utilization of MFH in human trials.

An adiabatic data reconstruction protocol was developed that reduced the thermodynamic uncertainties by a factor of $\sim$ 3.

Studies revealed that SAR decreased with increasing sample concentration for water based ferrofluids, which was attributed to the enhancement of dipolar interaction. On the other hand, SAR was found to increase with sample concentration for oil based ferrofluids due to an increase in effective number of heat sources per unit volume.

The increased polydispersity of the larger sized nanoemulsion droplets ($\sim$ 200 nm) was found to drastically reduce SAR. SAR was also found to decrease by $\sim$ 50 % for emulsion droplets immobilized in a tissue mimicking agar matrix due to the abrogation of Brownian relaxation.

Samples textured in the direction parallel to the RF-AMF showed $\sim$ 20-30% enhancement in SAR due to an enhancement of effective uniaxial anisotropy energy density.

Reported by
Dr. B. B. Lahiri
Metallurgy and Materials Group

Young Researcher's FORUM

CFD Investigations of Thermal Hydraulic Characteristics and Consequences of Flow Blockage in Fast Reactor Fuel Subassemblies

M. Naveen Raj did his B.E Mechanical Engineering from Magna College of Engineering under Anna University. He joined RDG/IGCAR as JRF in July 2012 and registered for his PhD in HBNI under the guidance of Dr. K. Velusamy. In September 2018, he successfully defended his Ph.D thesis titled "CFD investigation of thermal hydraulics characteristics and consequences of flow blockage in fast reactor fuel subassemblies". His areas of expertise are Conjugate Heat transfer, two-phase flow and phase change modeling.

Helical wire-wrapped fuel pins of sodium cooled fast reactors (SFR) are subjected to high heat flux of $\sim$ 2MW/m^2 and hence the fuel clad faces sustained high temperature leading to large creep damage. The gap between the hexcan wall and peripheral pins offers a low resistance flow passage compared to the central region, causing significant flow bypass towards the peripheral subchannels (SC). Apart from supporting the fuel pins against flow induced vibrations, the spacer wires induce prominent transverse flow. As consequences of these, there are periodic flow variations in the subchannels along the stream-wise direction. Also, the clad is subjected to significant temperature variations around the circumference leading to thermal stress in the clad. Characterization of local flow is very important for development of improved subchannel analysis codes and for optimizing the future design of subassembly. Presence of a large number of tiny subchannels enhances the possibility of blockage development in fuel subassemblies. Any possible blockage would have adverse impact on the availability and safety of the reactor. There is a strong need to understand the consequences of possible blockages (both planar and columnar types).

Computational Fluid Dynamics (CFD) simulations of a prototype fuel pin bundle with helical wire wrap (Figure 1), needs large computational resources. However, this requirement can be optimized, by adopting a structured mesh (Figure 2) and parallel computations. The structured mesh of the wire wrapped pin bundle has been generated using a customized mesh generator module. For the seven helical pitches considered for the prototype fuel subassembly, the entire domain is axially divided into 84 blocks and handled separately by 84 processors on a cluster computer with 48 GB RAM and 131 GFLOPS speed for each node.
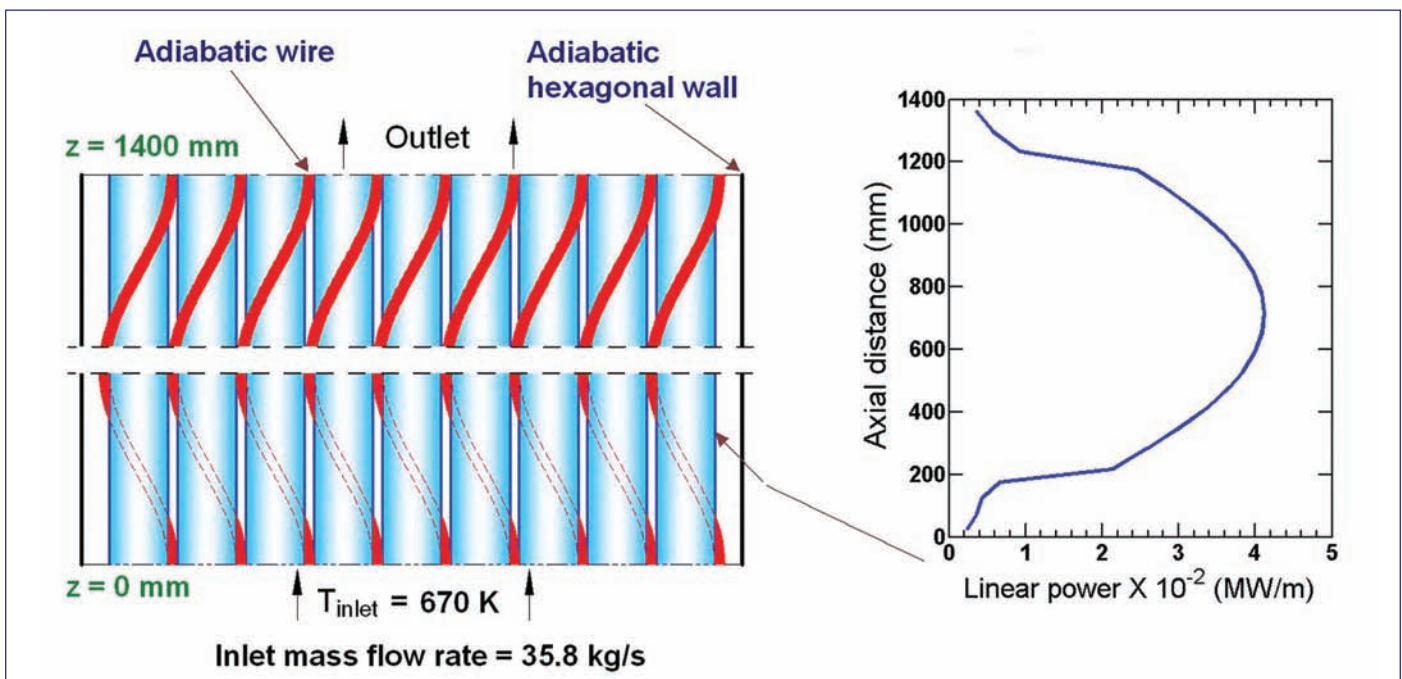

Figure 1: Wire-wrapper SFR fuel bundle (left) and axial heat generation profile (right)
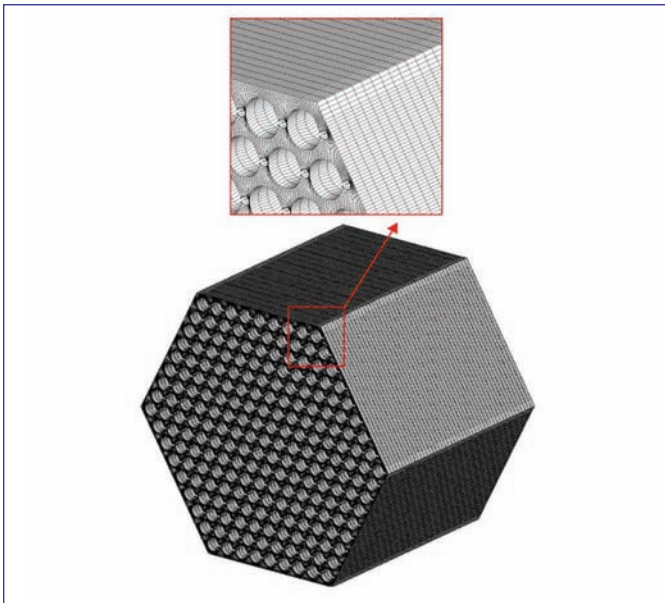
Figure 2: Mesh pattern in one pitch length (200 mm) of 217 pin bundle.

Subassembly Flow Features

Though the predominant flow in a wire wrapped subassembly is in the axial direction, presence of helical wire generates significant transverse flow, which results in spatially varying axial flow within each subchannel. Based on detailed investigation of fully developed flow in wire wrapped pin bundle, the following four characteristics are found.

(a) Axial flow rate variations: The axial flow rate through a subchannel is not constant and is superimposed with a periodic variation. The amplitude and phase shift of axial flow variations vary among subchannels in different radial and sectorial locations.

(b) Swirl around hexcan: There exists a unidirectional transverse swirl adjoining the hexcan wall, in the direction same as that of wire rotation around the pin.

(c) Flow bypass: There is diversion of flow towards the gap between the peripheral pin and the hexcan wall, where the resistance is low compared to that of the central region.

(d) Alternate inflow and outflow in peripheral subchannel: Alternate transverse inflow into peripheral subchannel from the center and outflow from peripheral subchannel towards the center persists in the entire length of the bundle.

The influence of helical wire on 3-dimensional flow field existing in the subassembly and the flow variation can be divided into,

- Local phenomenon: This is due to the passage of wire through a subchannel and its influence is localized to that subchannel.

- Global phenomenon: This is due to the change in orientation of wire with respect to hexcan wall in the peripheral region and its influence is visible in the whole sector.

Flow features in central and peripheral subchannels are widely different, because the strengths of these two phenomena vary among these two regions. Flow features in middle region are nearly similar to that of the central region and the flow features of outer region are closer to that of the peripheral region. For a quantitative and qualitative understanding of flow features within a subassembly, subchannels located in the various regions are investigated.

Axial flow variations in central subchannels

It shall be indicated that within an axial length of one helical pitch, three helical wires corresponding to the three pins that form the subchannel pass through the subchannel. The cross section area of a spacer wire is ~17% of the subchannel flow area. Hence, mass flow rate within the subchannel periodically changes attaining three minima. The spatial variation in axial mass flow rate within the same subchannel to the extent of ~21% is found.

Transverse velocity correlation for central subchannel

The transverse velocity fields in the central subchannel for four different wire angle positions are depicted in Figure 3. The subchannel under consideration is 1A. The predicted transverse mass flow rates through all the three faces as a function of wire angle are depicted in Figure 4. The algebraic sum of net influx through all the three faces is also depicted in the same Figure. As already indicated, for the development of an advanced subchannel model for SFR fuel subassembly, knowledge of transverse flow exchange among the subchannels is important. Hence, attention needs to be focused towards this. It is known that the helical wire wrap will try to sweep the flow along its direction of rotation. So, the transverse flow near the wire will be a function of axial velocity and wire helix angle. By splitting the components of velocity vector with respect to wire helix angle and assuming that the flow follows the wire exactly, the non-dimensional transverse velocity should be,

$$\frac{V_t}{V_a} = \frac{\pi(D + D_w)}{H}$$

But the maximum non-dimensional transverse velocity predicted by the CFD code is about 1.5 times this value. This could be attributed to the influence of other wires entering the subchannel and ejection flow near the wire wall. The non-dimensional transverse velocity across the subchannel face can be written in a generalized form as,
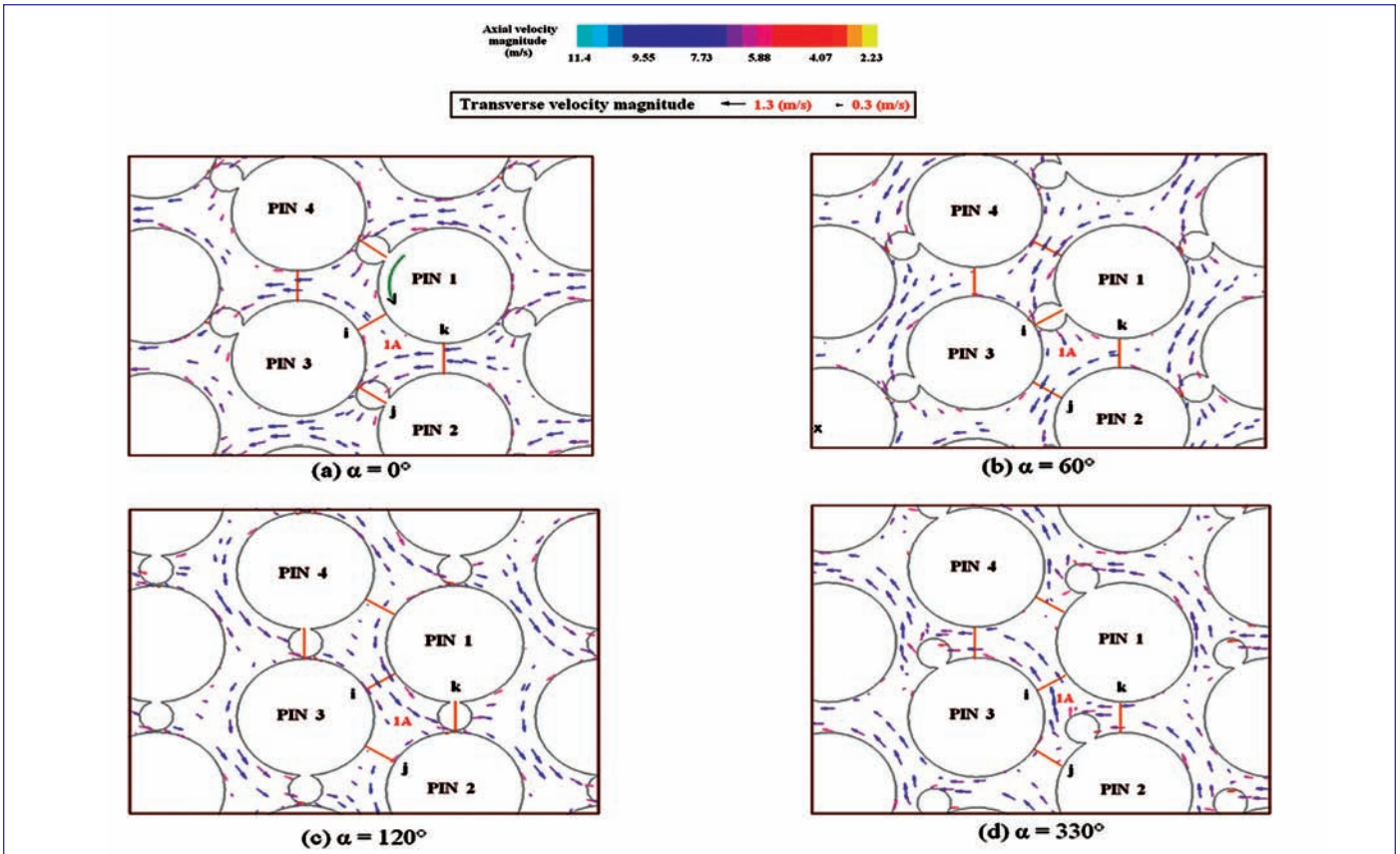
Figure 3: Transverse velocity vector in central subchannels at four different wire angles.

$$V_t^* = V_{max}\cos(\alpha) + N\left(\frac{V_{max}}{2}\right)\cos(6\alpha)$$

$$V_{max} = 1.5\left(\frac{V_t}{V_a}\right)$$

where,

This expression has two terms. The first term exists throughout the pitch, while the second term comes into picture when wire enters or leaves the subchannel through the corresponding face. For example, when the wire leaves the subchannel 1A through face k, N = 1, for (110° > α > 130°). Similarly, when the wire enters the subchannel 1A through face k, N = - 1 for (290° > α > 310°). For other angles, N = 0.

Further the axial variation of clad temperature in various pins is shown in Figure 5. It is seen that the pins in the central and middle regions do not exhibit any spatial variation in clad temperature. But,
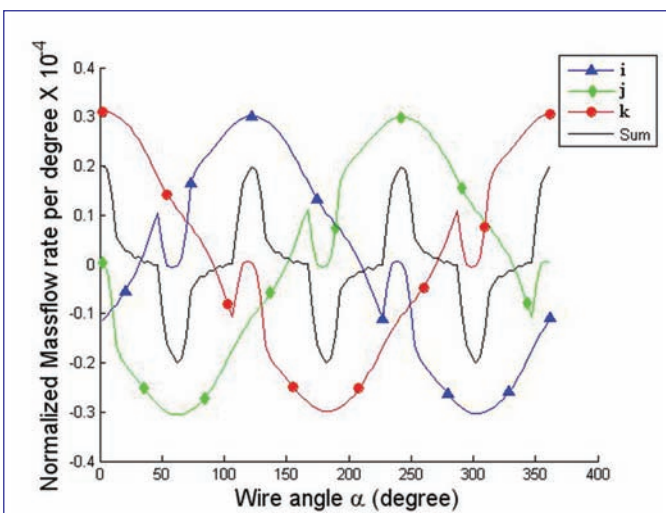

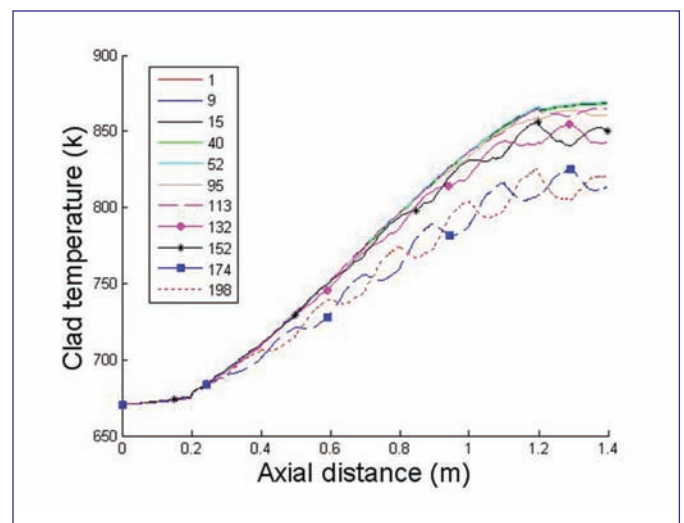Figure 4: Transverse mass flow rate per degree wire angle in a central subchannel

Figure 5: Clad temperature variation along the axial distance for various pins

pins in the outer and peripheral regions exhibit prominent variations with amplitude increasing in downstream direction. As seen in the transverse flow in the edge subchannel, there is a continuous influx of coolant into the edge subchannel from the core of the subassembly for α = 15°- 165°. The hot sodium coming from the central region flows over the peripheral pins keeping the clad at a comparatively high temperature. Similarly, there is a steady efflux in the edge subchannel for α = 195° to 345°. As a result of this, cold sodium from the vicinity of hexcan wall flows over the peripheral pins, keeping the clad temperature to be low in these wire orientations. A similar phenomenon influences the subchannel in the outer region.

Validation of CFD Model for Porous Blockage Simulations

The models adopted in the present analysis are validated with a physically similar experiment on a 19 pin wire wrapped bundle (Figure 6) with porous blockage. In the experiment, totally 44 thermocouple were employed in the blocked zone. Thermocouples were located both upstream and downstream of the blockage as well as within the blockage. The circumferential average of thermocouple readings at any plane within the blockage is compared with the corresponding computational results and presented in Figure 7. The comparison was found to be highly satisfactory.

Subassembly with Blockage

In SFR fuel clad, when there is sodium boiling, clad failure is imminent. Hence, attention is focused on the peak clad temperature
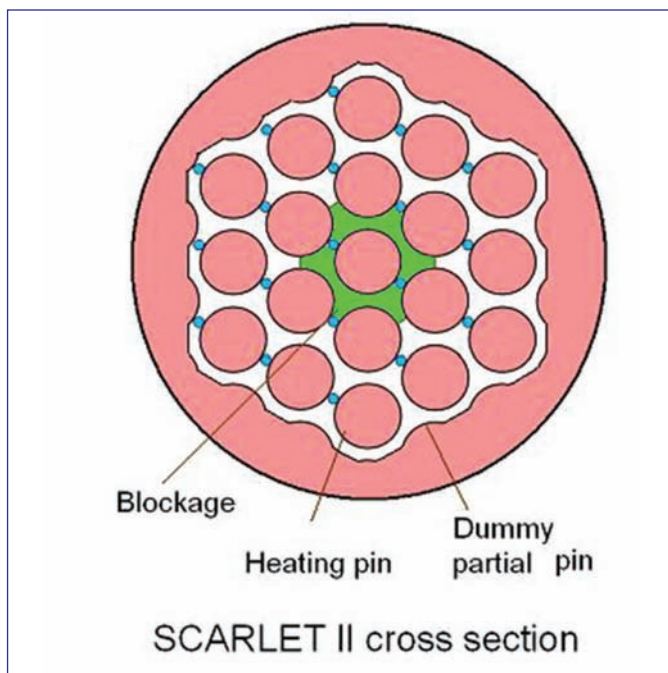
(hot spot) for fixing the critical blockage length for initiation of sodium boiling. This critical length for different types of blockages (porous columnar as well as non-porous planar) is found on the basis of parametric calculations. Critical length for which boiling is initiated for different radial extents and porosity, and particle diameter of blockage is found out and safe operating regime has been established.

Detectability of Blockage

Traditionally, sodium temperature exiting from every fuel subassembly is continuously monitored. A 10 °C rise in the sodium temperature leads to automatic reactor trip, while a 5 °C rise provides alarm. These rises in outlet sodium temperature correspond to flow reduction of 6 and 3% respectively. It was seen that the maximum reduction in flow rate is < 2.5 % among the various cases analyzed. Thus, presence of internal porous blockages cannot be detected by global subassembly outlet temperature monitoring, before the onset of boiling. Figure 8 shows, sodium temperature and axial velocity profiles at the exit of the bundle for unblocked and blocked bundles. It could be seen that for an unblocked case the temperature profile is almost uniform throughout the section, whereas large peak in sodium temperature occurs in the case with blockage. Larger the radial extent of blockage, higher is the magnitude of the peak temperature. The peak outlet temperature in a four row blockage is 160 K higher than that in unblocked case. This large local peak in the outlet sodium temperature could be used as a source for early deduction of the blockage, even though bulk outlet temperature could not be differentiated.

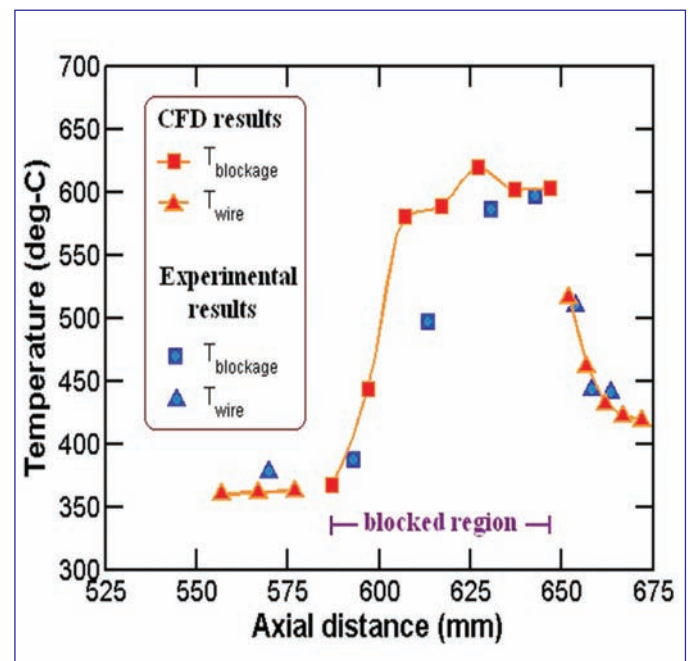Figure 6: Cross sectional layout of SCARLET II bundle with blockage

Figure 7: Comparison of predicted sodium temperature with SCARLET II measurements
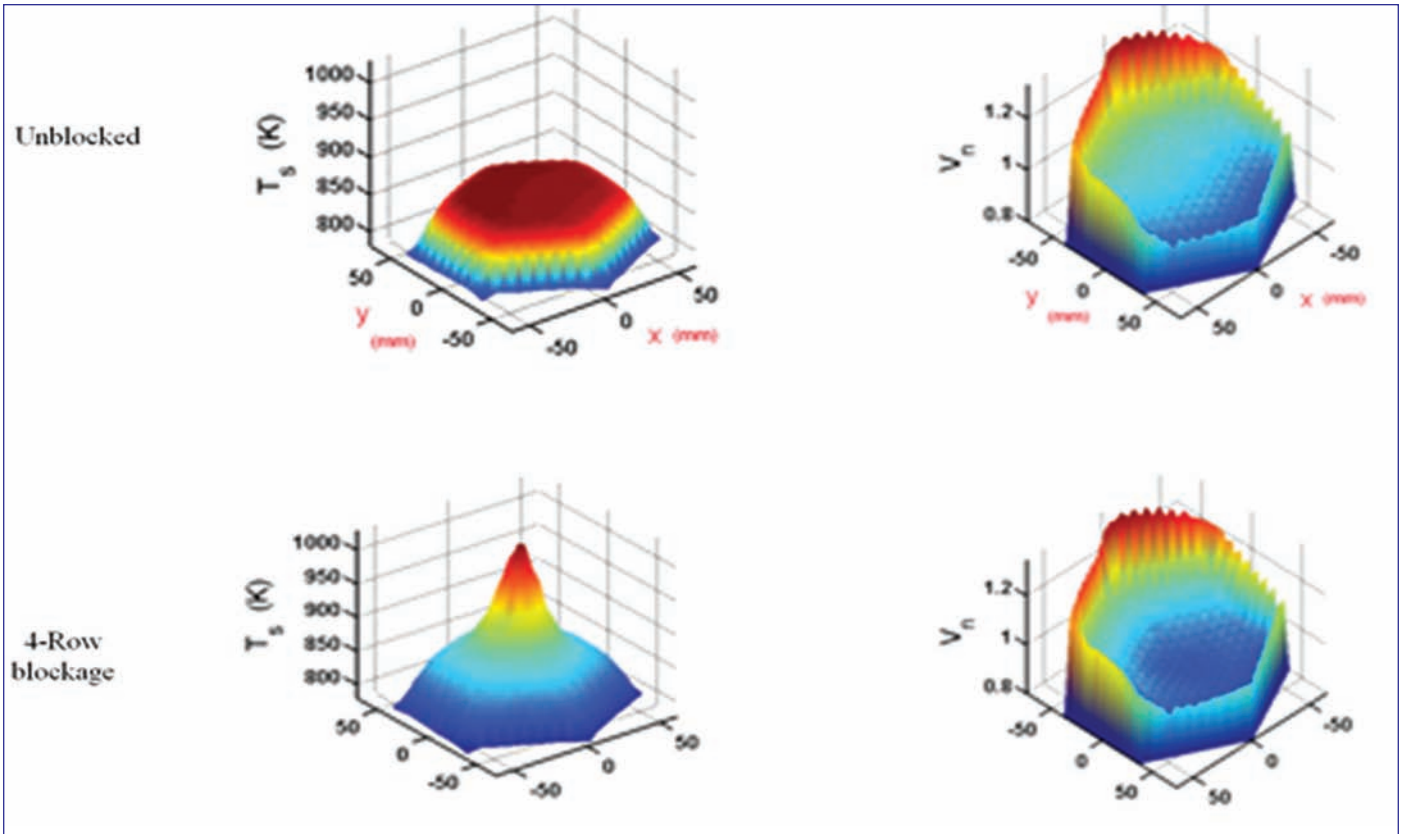
Figure 8: Comparison of temperature and velocity profiles at an elevation of 1300 mm from the inlet for unblocked and blocked cases

Thermal hydraulic features of fuel subassemblies have been investigated through computational fluid dynamics approach. Under normal conditions, the axial mass flow rate in any subchannel exhibits periodic spatial variations in the fully developed region of the bundle. The periodicity of axial flow in a central subchannel is 1/3rd pitch of helical wire. The origin of these periodic variations found is change in flow area and hydraulic resistance of the subchannel due to the passage of helical wire in the subchannel. In the central subchannels, the transverse flows crossing the subchannel lateral faces follow a cosine profile in the axial direction. These flows in different faces are identical but with a phase shift of 120°. Through the lateral faces of the edge subchannels facing the subassembly centre, a continuous inflow prevails for one half of the pitch while a continuous outflow prevails for the other half of the pitch. This causes larger amplitude axial flow oscillations in the peripheral subchannels compared to that in the central subchannels. Based on the predicted CFD results, correlations have been proposed for non-dimensional transverse velocity as a function of wire orientation, for various types of subchannels. These correlations can be adopted for development of advanced subchannel models for subassembly thermal hydraulic design.

Thermal hydraulic features of blocked fuel subassemblies with various porous / planar blockage configurations have also been investigated. A wide range of blockage radius, porosity, mean particle diameter and location of blockage has been considered. The critical length of blockage that would result in local sodium boiling as a function of aforementioned blockage parameters has been estimated. Subsequently, the parametric zone posing risk of sodium boiling has been determined. For a prototype subassembly, the total flow reduction due to porous blockage is found to be < 2.5 % for all blockages that can lead to local sodium boiling. This suggests, that global bulk sodium temperature monitoring at the outlet of the subassembly is unlikely to detect slowly growing internal porous blockages. Comparing the sodium flow and temperature fields in unblocked and blocked bundles, it is found that, the wake induced, temperature non-uniformity persists even up to 3 helical pitch lengths. This suggests that the sodium temperature non-uniformity at the bundle exit can serve as an efficient blockage indicator, provided the cross section temperature is mapped by a proper instrumentation.

Reported by
M. Naveen Raj
Reactor Design Group

Conference and Meeting Highlights

A brief report on One day Training Program on
Quality Assurance Aspects for Engineers and Supervisors

January 10, 2019

Dr. A. Ravisankar, Project Director, FRFCF delivering the Inaugural Address and Dr. B. P. C. Rao, CPE, FRFCF explaining the genesis & structure of the in-house Program

A one day in-house training program on Quality Assurance (QA) aspects during construction of Fast Reactor Fuel Cycle Facility (FRFCF) project was organized on January 10, 2019 for the benefit of engineers and supervisors of FRFCF. Shri D. Herbert, Additional Chief Engineer welcomed the participants and Dr. B. P. C Rao, Chief Project Engineer explained the genesis & structure of this training program and its necessity in FRFCF. Dr. A. Ravisankar, Project Director inaugurated the program and emphasized, in his inaugural address, the importance of QA in construction & design activities and the benefits that accrue. He requested the participants to utilize this unique opportunity for enhancing their understanding and knowledge in QA in their own domain as well as in other domains.

The program consisted of lectures covering the QA basics, methods and standards followed during construction. A hand-out of important aspects of these lectures was given to all the participants. Shri M.V. Kuppusamy covered QA aspects during Mechanical Fabrication & Construction and Shri V. Venkatachalapathy gave a detailed account of QA during Civil Construction. Shri B. Sasidhar Rao delivered a lecture on QA of Electronics & Instrumentation and Equipment & Systems and Shri S. Pothiraj explained the QA aspects of Electrical Equipments and Systems during construction. The training program was attended by about 65 engineers and supervisors. A good interaction and lively discussions were observed between the speakers and the participants. In the end, feedback was solicited from the participants. Participants mentioned that the talks were informative and useful and requested the organizers for a repeat course spanning two days.

Reported by
B. Sasidhar Rao, FRFCF

Conference and Meeting Highlights

International Women's Day & The International Year of Periodic Table-2019

March 8, 2019

Presentation being made on the occasion of "International Women's day" and "International Year of Periodic Table -2019"

On March 8 of every year, UN Women, the United Nations entity is observing International Women's Day to celebrate the global push for gender equality and to make women's rights a reality. To commemorate this year's theme, "Think Equal, Build Smart, Innovate for Change" and "The International Year of Periodic Table-2019" declared by the UNESCO, a technical program covering the discovery of elements along with their applications in various fields was arranged and presentations were made by women employees and research scholars of Materials Chemistry & Metal Fuel Cycle Group.

Dr. T. Prathibha welcomed the gathering. In the inaugural address, Dr. K. Ananthasivan, AD, MFCG highlighted the importance and respect for women in our culture and also recalled the great contribution of the family of Nobel laureate Marie Curie. Ms. Lithun Swain reviewed the contribution of the women to the periodic table by explaining the role of women in the discovery of elements. Ms. Beatrice Veena discussed the discovery of hydrogen and its isotopes in the chronological order and covered the application of hydrogen in various fields including her work on hydrogen sensor. Ms. J. Vithya described about the discovery of strontium, the advantage of production of radioisotopes of strontium and cobalt in the Fast Breeder Test Reactor and their medical applications especially in the treatment of cancer. Ms. S. Annapoorani described the fortuitous discovery of iodine from seaweed, the importance of iodine to health, its toxicity and the studies being carried out on trapping of iodine using Ag modified zeolite towards nuclear application. Ms. Subrame Sarkar highlighted the discovery of plutonium and described the work of extraction of actinides and other fission products carried out at MC&MFCG. The work-life balance for women was discussed by Ms. S. Nalini with the suggestions to prioritise the activities, delegation of activities, etc. A quiz program covering the 'First Woman of India' in various fields was conducted in between the sessions by Ms. Clinsha. Dr. S. Vijayalakshmi, Head, ACS, Materials Chemistry Division mentioned the need to improve the capabilities of women, the role of innovation in the employment and concluded that collective action by both men and women is required for the accelerated growth of women in employment. Dr. Kitheri Joseph, Head, MFC&PS, MFFD coordinated the panel discussion on leadership qualities of women. Ms. Nibedita Samanta proposed the vote of thanks.

Reported by
Dr. S. Vijayalakshmi, MC&MFCG

News and Events

Swachhta Pakhwada - 2019
February 16-28, 2019

Cleaning of Office premises

Visit by the members of Swachhta Cell

News and Events

Shri M.S.Premnath, Superintending Engineer (Retired), Chennai Corporation during the closing ceremony

 IGCAR observed "Swachhta Pakhwada" during February 16-28, 2019. Scrap, with special emphasis on e-waste, was disposed and office premises were cleaned. In order to provide a boost to the swachhta activities, members of IGCAR Swachhta Cell visited various Divisions/Groups and selected three best kept locations. Certificate of Appreciation was awarded during the closing ceremony of Swachhta Pawkhwada. A guest lecture by Shri M.S.Premnath, Superintending Engineer (Retired), Chennai Corporation on "Managing Waste" was organized on the closing day. Essay, slogan and poster competitions on the topic "Clean and Green Environment" were conducted and prizes distributed during the closing ceremony.

Reported by
O.T.G. Nair, Director, P&A

Shri Anil Swarup, Former Secretary to Government of India delivered IGC Colloquium on "Making Things Happen in India" on March 18, 2019

News and Events

The official language implementation committee (OLIC), IGCAR organised a one-day scientific seminar on the subject *'Clean Energy, Environment and Advance Technologies'* through Hindi medium on January 10, 2019 at Sarabhai Auditorium. A summary of all the presentations in the form of a booklet, *Saraansh Pustika* was released by Dr. Arun Kumar Bhaduri, Director IGCAR and Chief Guest, during the inaugural function. Best paper and poster presentations were awarded cash prizes.

HBNI-IGCAR Corner

Research Contribution Awards

Effect of Parameterized and Explicit Convection Physics Schemes on the Simulation of Tropical Cyclones Over the Bay of Bengal
Ms. Reshmi Mohan
International Workshop on Modelling Atmospheric -Oceanic Processes for Weather and Climate Extremes (MAPEX-2019) held at IIT, Delhi, March 28-29, 2019.
Third best poster award

Shri Santanu Kumar Parida Received the Ovshinsky Student Award during March 2019 APS Meeting held at Boston, USA

Shri Surojit Ranoo - His popular story entitled "Magnetic Nanoparticles Hyperthermia: An Emerging Cancer Therapy Sans Side Effects" has been selected (One among hundred) under Ph.D category for Augmenting Writing Skills for Articulating Research (AWSAR) Award 2018, Deapartment Science and Technology, Government of India.

Ph.D Thesis Defense

Name	Title	Date	Discipline
Mr. M. Bootharajan	Studies on Preparation and Characterization of Some Ytterbium Substituted Zirconates and Thorates	22-02-2019	Chemical Sciences
Ms Soja Vijay	Studies on the Synthesis and Sintering of Nanocrystalline B_4C and YSZ	07-03-2019	Chemical Sciences
Mr. Suranjan Bera	Mass Spectrometric studies on some Materials of Relevance to Nuclear Technology	15-03-2019	Chemical Sciences
Ms Annapurna Rout	Study of Uranium Luminescence in Borophosphate and Borate Hosts	29-03-2019	Chemical Sciences
Mr. M. Vairavel	Experimental and Ab-initio Studies on Solute-defect Interactions in Fe and FeCr alloy	11.01.2019	Physical Sciences
Mr. Deepak Kumar Gupta	Design and Development of Holographic Optical Tweezers and Studies on Colloidal Systems	21.01.2019	Physical Sciences
Mr. C. Lakshmanan	Investigation of Defects and Microstructure in Nanoporous Au	07.02.2019	Physical Sciences
Mr. Pramod Kumar Sharma	A Study on the Reliability of Class III Power Supply System of A Sodium Cooled Fast Breeder Reactor Under Internal and External Events	18.02.2019	Physical Sciences
Mr. A. W. Zaibudeen	Investigation on the Behavior of Stimuli-responsive Macromolecules at Nanomulsion Interface	25.02.2019	Physical Sciences
Mr. Padi Srinivas Reddy	Remote Online Performance Evaluation of Radiation Monitors in Nuclear Plants	02.01.2019	Engineering Sciences
Mr. G. Padmakumar	Thermal Hydraulics of SFR Fuel Bundle with Inserts in Peripheral Subchannels	12.02.2019	Engineering Sciences
Mr. A. Moorthi	Investigations of Coolant Mixing in Nuclear Reactor Fuel Pin Bundles	15.02.2019	Engineering Sciences
Mr. G. Prasanna	Development of Embedded Readout and Design Optimization of PIN Diodes for Radiation Detection	07.03.2019	Engineering Sciences

Best Paper/Poster Awards

DST National Conference on Nanomaterials, held during 24 - 25, January 2019, at LRG Government Arts College for Women, Tiruppur, India.
Probing of Nanofiller-Polymer Matrix Interaction Using Atomic Force Microscope for the Development of X-ray opaque Fabric Material. Shri M. Vadivel, Ms. Sangeetha Jayakumar, Dr. John Philip
Best Paper Award

5th International Conference on Nanoscience and Nanotechnology, ICONN 2019 held at SRM University Chennai during 28-30, January 2019.
Carbon black and nickel nano inclusions assisted thermal conductivity enhancement of an organic phase change material for thermal energy storage. Shri Amit Kumar Mishra, Dr. B. B. Lahiri, Dr. John Philip
Best Poster Award

Biodiversity Basket - Avian Fauna

Ashy Prinia

The Ashy Prinia is a small warbler. It is a common bird in both Kalpakkam and IGCAR campus and its small size, distinctive colors and upright tail make it easy to identify.